Lawrence Berkeley National Laboratory
LBL Publications

Title
Surfactant inhibition mechanisms of carbonate mineral dissolution in shale

Permalink
https://escholarship.org/uc/item/8kr637ck

Authors
Kim, Kyung Tae
Jagannath, Mantha Sai Pavan
Su, Gregory M
et al.

Peer reviewed

1   **Surfactant Inhibition Mechanisms of Carbonate Mineral Dissolution in Shale**

2

3   Kyung Tae Kim[1], Mantha Sai Pavan Jagannath[3], Gregory M. Su[4], Guillaume Freychet[5],

4   Tongzhou Zeng[2], Kishore K. Mohanty[2], Graeme Henkelman[3], Lynn E. Katz[1], Charles J. Werth[1,*]

5

6   [1] 301 East Dean Keeton St., Department of Civil, Architecture & Environmental Engineering,

7   University of Texas at Austin, Austin, TX, 78721, USA

8   [2] 200 East Dean Keeton St., Hildebrand Department of Petroleum & Geosystems Engineering,

9   University of Texas at Austin, Austin, TX, 78721, USA

10   [3] 2506 Speedway Dr., Department of Chemistry, University of Texas at Austin, Austin, TX,

11   78721, USA

12   [4] Advanced Light Sources, Lawrence Berkeley National Laboratory, Berkeley, CA 94720, USA

13   [5] National Synchrotron Light Source II, Brookhaven National Laboratory, Upton, NY, 11973,

14   USA

15

16

17   *corresponding author: werth@utexas.edu

18

19   **ABSTRACT**

20   Surfactants are common additives to hydraulic fracturing and enhanced oil recovery (EOR) fluids,

21   and are under consideration for amendment to supercritical carbon dioxide for geological carbon

22   sequestration (GCS). The effect of a common anionic surfactant, internal olefin sulfonate (IOS),

23   on mineral dissolution from shale into brine was evaluated. When added to brine at concentrations

24   exceeding the critical micelle concentration (94 mg/L), IOS inhibited carbonate mineral

25   dissolution in an Eagle Ford shale, as well as dissolution of optical quality calcite (the dominant

26   carbonate in the shale). Laser profilometry images provide spatial resolution across >3 orders of

27   magnitude, and indicate that IOS addition to brine both enhances the formation of new etch pits in

28   calcite, and impedes their further growth. Time-of-flight secondary ion mass spectrometry surface

29   profiles show for the first time that IOS preferentially adsorbs at calcite pit edges versus flat calcite

30   surfaces (i.e., terraces). Surface pressure calculations, sulfur K-edge near edge X-ray absorption

31   fine structure (NEXAFS) spectroscopy results, and density functional theory (DFT) calculations

32   support this observation; the DFT results indicate that the sulfonate head group of the IOS

33   molecule binds strongly to the calcite step site as compared to the terrace site. The S K-edge

34   NEXAFS results indicate that IOS adsorbed more to etched calcite surfaces compared to smooth

35   calcite surfaces. Overall, the results indicate that weak adsorption on flat calcite surfaces (i.e.,

36   terraces) disrupts water structure and enhances mass transfer of dissolution, while strong

37   adsorption on calcite pit edges displaces adsorbed water and inhibits further etch pit growth. This

38   work provides the first direct evidence of preferential adsorption of IOS to etched calcite surfaces

39   and links it to macroscopic dissolution kinetics. This work has implications for surfactant-

40   containing fluids used in hydraulic fracturing, EOR and potentially GCS for subsurface injection

41   into carbonate rich reservoirs.

42

43   **Keywords**

44   Eagle Ford Shale, Calcite, Anionic Surfactant, Density Functional Theory, Time of Flight

45   Secondary Ion Mass Spectrometry, near edge X-ray absorption fine structure spectroscopy

46

47

48

1. Introduction

Shale formations have emerged as critical stratigraphic units in unconventional hydrocarbon recovery [1,2] and geological carbon sequestration [3,4]. In the former they are rich sources of oil and natural gas, and in the latter they serve as cap rock to prevent carbon dioxide escape. Shales are complex assemblages of fine mineral fragments and organic matter of varying reactivity [5], and in many cases are dominated by highly reactive carbonate minerals (e.g., Eagle Ford shale > 60% calcite [6–8], Wolfcamp and Marcellus shales >80% calcite+dolomite). Shales are exposed to injected fluids during hydraulic fracturing and geological carbon sequestration leading to dissolution and secondary mineral precipitation. Dissolution has been shown to open pore spaces and fractures in shale matrices and create conduits for fluid flow [9,10], and to decrease geomechanical integrity [10,11]. The latter can weaken rock, promoting collapse as rubble and the closure of propped fractures, or promote slippage along grain and fracture boundaries inducing seismicity. A number of researchers have investigated the effects of water with varying pH, carbon dioxide partial pressure (PCO_2), and temperature on shale mineral reactions [3,9,12]. The effects of various additives have also been evaluated [13,14]. However, the effects of surfactants on mineral reactivity have rarely been addressed.

Surfactants are commonly added to hydraulic fracturing and enhanced oil recovery (EOR) fluids to reduce interfacial tension and to alter reservoir wettability [16,17]. Anionic, cationic, zwitterionic, and nonionic surfactants are all used in practice, and the type selected for use in a reservoir depends on many factors including formation mineralogy, salinity, hardness, pH, and temperature [18]. Surfactant head groups bind to oppositely charged sites on mineral surfaces via electrostatic forces, and this is aided by weaker van der Waal forces [19,20]; this is also aided by favorable entropy changes that occur when hydrophobic surfactant tails partition from brine to neutrally charged mineral surfaces and natural organic matter. Near neutral pH, carbonates (e.g., points of zero charge$_{calcite}$=8-9.5 [21]) are positive and this aids anionic surfactant sorption [22]. At low concentrations on mineral surfaces, individual and non-interacting surfactant molecules adsorb at the most favorable sites (e.g., edges) [23,24]. As concentrations increase, hemimicelles can form at these same sites, and at less favorable sites, and surfactant molecules can interact with each other. Above the critical micelle concentration (CMC), adsorption is independent of surfactant concentration. Surfactants have been used to protect metal surfaces from corrosion in

79   acidic solutions, with the assumption that they inhibit proton attack [25]. It follows that surfactants

80   might protect shale mineral surfaces from dissolution, but this has not been examined.

81   The ubiquity of carbonates in shales and other human-impacted systems (e.g., conventional

82   reservoirs, potable groundwater aquifers, soil, biological systems, and engineered structures) has

83   motivated study of their reactivity under widely varying conditions [26,27]. Among the most

84   studied carbonate is calcite, and its dissolution is of interest in this study. Broadly, calcite

85   dissolution occurs by surface etching, where bound calcium and carbonate ions are solubilized on

86   calcite surfaces preferentially at defect sites such as step edges and edge kinks [28–31]. Various

87   rate laws and mechanisms have been proposed to describe calcite dissolution rates. In relatively

88   pure water, dissolution rates have been related to proton (a_{H^+}), carbon dioxide ($a_{H_2CO_3^*}$), water

89   (a_{H_2O}), calcium ($a_{Ca^{2+}}$), and bicarbonate ($a_{HCO_3^-}$) activities via eq 1 [32].

90    $$R = k_1 a_{H^+} + k_2 a_{H_2CO_3^*} + k_3 a_{H_2O} - k_4 a_{Ca^{2+}} a_{HCO_3^-} \qquad (1)$$

91   where $[H_2CO_3^*]=([CO_2(aq)] + [H_2CO_3^o])$. Below ~pH 3.5 the first term on the right hand side of

92   eq 1 dominates. At higher pH, the forward reaction is governed by the second and/or third term

93   depending on pCO$_2$ and pH. The reverse (precipitation) reaction (fourth term) becomes important

94   as the solution approaches saturation with respect to calcite. When the third term dominates,

95   dissolution is sufficiently slow such that mass transfer to the calcite surface can be ignored.

96   Many studies have evaluated the effects of aqueous constituents on calcite growth and

97   dissolution, with the greater focus on inorganic ions. Both inhibition (e.g., organic acids, Fe^{2+},

98   Mg^{2+}, Sr^{2+}, PO_4^{3-}) and enhancement (e.g. chelators, Cl^-, I^-, F^-,) of dissolution kinetics have been

99   observed [33–42], and in some cases enhancement changed to inhibition or vice versa as the

100   concentration and/or molecular weight of structurally similar molecules changed (e.g.,

101   polyaspartate) [43,44]. Inhibition kinetic effects are often attributed to ion adsorption and pinning

102   at step edges [33], as well as general competitive adsorption with Ca^{2+} and/or CO_3^{2-} [35]. Inhibition

103   has also been related to incorporation of metal impurities into the carbonate mineral [36,45].

104   Enhancement of the kinetics is less common, but has been attributed to disruption of the adsorbed

105   water layer at the calcite surface with possible lowering of the energy barrier for etch pit nucleation

106   and enhanced mass transfer [43,44,46].

107   Aqueous constituents also affect calcite etch pit geometry. Rhombohedral etch pits ideally

108   form on $\{10\bar{1}4\}$ surfaces in pure water. These pits primarily grow by dissolution of Ca^{2+} and CO_3^{2-}

109   along acute and obtuse edges, and growth along obtuse steps is faster in pure water [28]. Inorganic

ions have been shown to favorably adsorb at acute or obtuse edges, and thereby promote growth of etch pits in one or the other direction [33,36]. The effects of adsorbed organic ions appear even more complex and have been extensively studied in the field of biomineralization. Organic molecules containing amino acid or carboxyl groups bind with calcite surface and step edges by stereochemical recognition, resulting in macroscopic etch pit morphology modification or stabilization of different crystal facets [30,43,47–49]. Poly-n-aspartic acid, for example, was shown to preferentially adsorb to acute edges for n=1, 2, and obtuse edges for n=3, 4, 6 [43], thereby promoting growth in opposite directions. Also, different enantiomers of aspartic acid (i.e., D- and L-) adsorb at opposite acute edges of etch pits and yield different mirror image etch pit geometries [30]. The effects of surfactants, which have different hydrophilic functional groups (e.g. sulfonate) that can potentially interact with mineral surface and also hydrophobic chains that induce complex adsorption behavior by forming micelles, on calcite dissolution rates and etch pit morphologies have received little attention.

The objectives of this study are to determine which component(s) of shale are most reactive with a simplified model brine (0.4 M KCl) at circumneutral pH and low total carbonate (C_T) under ambient pCO_2, whether an anionic surfactant protects shale mineral component(s) from dissolution, and to identify the mechanisms of this protection. To address these objectives, dissolution kinetics of an Eagle Ford shale were measured under ambient conditions in brine without and with the anionic surfactant internal olefin sulfonate (IOS). Dissolution results and geochemical modeling were used to identify which mineral(s) reacted and were protected by IOS. Calcite was identified as the primary mineral protected by IOS from dissolution, and the dissolution kinetics of optical quality calcite were similarly measured and complemented with laser profilometry images of resulting etch pit geometries. Calcite-brine surface pressure values were determined from wettability measurements. Site specific distribution of IOS on calcite surfaces was evaluated with time-of-flight secondary ion mass spectrometry (ToF-SIMS), and further probed with near edge X-ray absorption fine structure (NEXAFS) spectroscopy and density functional theory (DFT) calculations. These different methods provided multiple lines of evidence to interpret the mechanisms affecting calcite dissolution inhibition by IOS.

2. Experimental

2.1   Materials

141   Most stock chemicals received were reagent grade. They include 1M HCl (Aldrich® 99.99%),

142   HNO$_3$ (Fisher, Trace metal grade), 1N KOH (J.T.Backer, analytical grade), and solid KCl

143   (Aldrich®, 99%). A 30.1 wt% anionic surfactant solution of internal olefin sulfonate (IOS C15-18)

144   was obtained from Shell Oil Company (product number O332); the structure is shown in Figure

145   1a. A core sample of oil-wet shale from a burial depth of 3,400 m was obtained from the Eagle

146   Ford reservoir in south Texas. Optical quality calcite crystals from Brazil and gypsum crystals

147   were purchased from Ward's Scientific. Ultrapure water was prepared from a Thermo Scientific

148   Barnstead Nanopure Model 7143, and it was characterized by a resistivity of 18.2 MΩ-cm.

149 **2.2   Brine and IOS Brine Solution Preparation**

150   Ultrapure water and powdered KCl were combined to make a 0.401 M KCl solution, hereafter

151   referred to as brine solution. This corresponds to an ionic strength of 0.401 M, which is similar to

152   lower values identified in Eagle Ford shale formation water.[50] The anionic IOS surfactant was

153   received and stored in a highly basic stock solution to maintain compound stability. It was chosen

154   because it is a common additive to both enhanced oil recovery and hydraulic fracturing fluids

155   [51,52]. The key roles of IOS in EOR and hydraulic fracturing are interfacial tension reduction

156   and reservoir wettability alteration. Just before use, the required amount of IOS stock solution was

157   diluted to 15,000 mg/L, then mixed with HCl to adjust the pH to 4.3. This pH reduction

158   transformed all carbonate species into carbonic acid (H$_2$CO$_3^*$). Subsequently, sonication and

159   vacuum were applied to degas dissolved CO$_2$ until no gas evolution was apparent. The pH of this

160   solution was then adjusted upward to >6 by adding 0.1 M KOH. The CO$_2$ removal by sonication

161   and vacuum was confirmed by acid titration with HCl. The pH-adjusted IOS stock solution was

162   then diluted into brine to obtain desired IOS concentrations (e.g., 500 mg/L and 3000 mg/L). The

163   pH values of all brine and combined IOS brine solutions were adjusted to 6.3 using 0.1 M HCl

164   before use.

165 **2.3   Eagle Ford Shale and Calcite Sample Preparation**

166   The Eagle Ford shale was used in powder form. Larger chunks of Eagle Ford shale were turned

167   into powder by grinding with a mortar and pestle. This powder was then rinsed in brine three times

168   by sequential centrifugation at 6000 rpm and decanting; this was done to remove very fine mineral

169   and organic matter particles that could pass through a syringe polyethersulfone (PES) filter during

170   experimental sampling (see next section). The decanted brine was discarded, and the retained

171   solids (>98%) were dried and then used in experiments.

172   The optical quality calcite was used as coarse grain particles, and in cleaved samples. Coarse
173   grain particles were created by first rough grinding using a mortar and pestle. Next, these particles
174   were passed through a #20 mesh sieve, and then collected on a #100 mesh sieve, to obtain the
175   desired size fraction (150-850 μm). These calcite particles were then quickly (minutes) rinsed by
176   sonicating in ultrapure water and decanted to remove very fine particles. Cleaved samples were
177   prepared by cleaving 2 mm thick by ~1 cm^2 calcite specimens from larger blocks of optical quality
178   calcite using a razor [53]. The cleaving exposed fresh $\{10\bar{1}4\}$ surfaces, and the cleaved samples
179   were immediately immersed in experimental solution (details below) to prevent surface
180   contamination and reaction with the atmosphere.

181   **2.4   Eagle Ford Shale and Calcite Dissolution Experiments**

182   Eagle Ford shale batch dissolution experiments were performed in 40 mL vials at 22 ± 1 °C by
183   submerging ~0.5 g of powered samples in 10 mL of brine alone or IOS mixed brine solutions
184   (hereafter referred to as IOS brine), and then sampling and analyzing for dissolved elements and
185   ions over time. The vials were loosely covered so that CO_2 could exchange between brine and the
186   atmosphere (open system), and then mixed with a stir bar. In most experiments, ~0.3 mL brine
187   samples were collected at 1, 3, 6, 12, and 48 hours. All aqueous samples were collected through a
188   0.22 μm syringe filter.

189   Calcite batch dissolution experiments were performed in 40 mL vials at 22 ± 1 °C by
190   submerging ~0.5 g of particles or cleaved samples in 10 mL of brine alone or IOS brine, and then
191   sampling and analyzing for Ca^{2+}, pH, and total carbonate over time. As before, the vials were
192   loosely covered so that CO_2 could exchange between brine and the atmosphere, and for calcite
193   particles the solution was continuously mixed. For all experiments, approximately 0.3 mL samples
194   were collected after 1, 3, 6, 12, and 36 hours, again through 0.22 μm filters.

195   Calcite etch-pit experiments were performed using only cleaved calcite pieces. In one set of
196   experiments, the cleaved calcite pieces were submerged in brine alone or IOS brine for 12 hours,
197   removed from solution and gently rinsed with ethanol to remove salts and adsorbed IOS, dried
198   with pure N_2, and then analyzed using laser profilometry. In another set of experiments, replicate
199   calcite samples submerged in brine for 12 hours were then subsequently transferred to either a
200   solution of only brine or a solution of IOS brine for another 12 hours. After this second aging
201   period, the samples were again rinsed with ethanol, dried with N_2, and evaluated using laser
202   profilometry.

203   All experiments were performed under ambient conditions, while reservoirs are typically under

204   high pressure and elevated temperature. Hence, this work represents a first step toward mechanistic

205   evaluation of surfactant effects on shale mineral dissolution, and further work under reservoir

206   conditions is warranted.

207   **2.5 Measurement of Ca^{2+} in Ion Exchange Sites**

208   The cation exchange capacity was measured following method proposed by Amrhein and

209   Suarez which is pertinent for calcite and/or gypsum rich soils [54]. Also, the amount of Ca^{2+} in ion

210   exchange sites at the start of Eagle Ford shale dissolution experiments was evaluated to distinguish

211   this contribution from dissolution of calcium-containing minerals. Briefly, powdered Eagle Ford

212   shale samples were rinsed three times in brine and then placed into a 0.5 M aqueous solution of

213    $MgCl_2$. The Ca^{2+} in solution was then measured. The Mg^{2+} will displace Ca^{2+} from cation exchange

214   sites, as well as promote mineral dissolution because it is under-saturated in calcium. The Ca^{2+}

215   displaced by Mg^{2+} is distinguished by subtracting the concentration of constituent ions (e.g., CO_3^{2-}

216   for calcite, SO_4^{2-} for gypsum) from the measured total Ca^{2+} concentration.

217   **2.6 Surface Tension and Contact Angle Measurements**

218   A Ramé-hart Model 500 Goniometer was used for surface tension and contact angle

219   measurements. Surface tension values were determined for brine and mixtures of IOS and brine

220   using the pendant drop method. The CMC of IOS also was determined by calculating an inflection

221   point from the surface tension vs log IOS concentration plot (Figure 1b). Contact angle values for

222   brine and IOS brine were determined by placing a drop of these liquids onto a freshly cleaved

223   calcite surface, and measuring contact angles from image analysis. The calcite surface was washed

224   between measurements following Costa and Aquilano [55]. Each surface tension and contact angle

225   value reported is the average of five different measurements.

226   **2.7 Elemental and Ion Analyses**

227   Elemental analysis was performed using a Varian 710-ES inductively coupled plasma – optical

228   emissions spectroscopy (ICP-OES) instrument. Lower detection limits for Ca and Mg are 0.03

229   μg/L and 0.1 μg/L, respectively. 100 μL of each sample collected from experimental vials was

230   diluted into 9.9 ml of Nanpure water mixed with 200 μL of concentrated nitric acid, and then

231   analyzed for Ca and Mg. The oxyanion sulfate (SO_4^{2-}) was measured using a Thermo scientific

232   Dionex ICS-2100 ion chromatograph (IC). 50 μL of each sample collected from experimental vials

7

233 was diluted into 0.95 ml of ultrapure water and analyzed. Solution pH was measured using a
234 Mettler Toledo pH electrode LE438. Carbonates were measured by acid titration using HCl.

235 **2.8 Surface area, Mineralogy, and Total Organic Carbon**

236 The specific surface area (SSA) of Eagle Ford shale was measured using N_2 adsorption with a
237 Micromeritics 3Flex Surface Area analyzer. Samples were analyzed over the pressure range from
238 0.73 to 748 mm Hg at 77 K, and analyzed using the Brunauer-Emmett-Teller isotherm. Mineralogy
239 and total organic carbon (TOC) of the Eagle Ford shale were measured by the commercial
240 laboratory, Premier Oilfield Group. The former was measured by X-ray diffraction (XRD) using
241 a Bruker D8 diffractometer, and the later by a total organic carbon analyzer using a Leco-carbon
242 analyzer.

243 **2.9 Laser Profilometer Analysis**

244 A Keyence VK-1100 Laser Profilometer was used to characterize surface morphology and pit
245 formation. Surface profiles were mainly collected with 50X lens to scan 211×281 μm^2. The vertical
246 display resolution is 0.5 nm, and the precision of repeated scans in the laser confocal mode with
247 the 20X lens is 40 nm. Depending on the size of the pits, higher magnification lenses were used.
248 Surface profiles were processed with VK-X series Multi-file Analyzer software. The reference
249 plain setting was first performed with a relatively flat surface, and then the depth and area of each
250 pit were measured by referencing the adjacent flat surface. The arithmetic average areal roughness
251 (S_a) was calculated over the scanned area.

252 **2.10   IOS Surface Location and Coverage on Calcite**

253 IOS surface location and coverage on calcite pieces was determined using Time-of-Flight
254 Secondary Ion Mass spectrometry (ToF-SIMS). Freshly cleaved calcite samples were aged in brine
255 for 12 hours to form etch pits. The brine was then mixed with IOS to reach 10 or 100 mg/L, and
256 allowed to incubate for 1 hour. Samples were then removed from solution, gently dried by blowing
257 ultrapure N_2, and placed in the ToF-SIMS instrument for analysis of the spatial distribution of IOS
258 (i.e., SO_2^-) and calcite (i.e., Ca^-, CO_3^-) containing molecular fragments. A calcite sample aged in
259 brine without IOS and in concentrated IOS on a silicon wafer were also analyzed as controls.

260 The specific instrument used was an ION-TOF (GmbH, Germany, 2010). During the
261 sputtering/analysis process, a Cs^+ sputtering ion beam (beam energy 500 eV, current ~ 40 nA), and
262 a pulsed Bi_3^+ cluster analysis ion beam (30 keV ion energy, 100 ns pulse duration) with either 3.7

263 pA (depth profiling) or 2.7 pA (high-resolution imaging) of measured sample current, were used.

264 Additional details are in Supporting Information.

265 Relative amount of IOS adsorbed on calcite with and without etch pits were determined using

266 near edge X-ray absorption fine structure (NEXAFS) spectroscopy. Concentrated IOS (30.1%) on

267 a silicon wafer and cleaved gypsum ($CaSO_4 \cdot 2H_2O$) were prepared as controls to determine energy

268 shift correction and type of sulfur functional groups in the IOS. A freshly cleaved calcite was also

269 analyzed as a control to investigate sulfur impurities. Four additional samples with two different

270 surface morphologies (i.e., etched or cleaved calcite) were prepared by first aging cleaved calcite

271 in brine or calcite saturated brine, respectively for 12 hours. The brine or calcite-saturated brine

272 was then mixed with IOS to reach 10 or 100 mg/L, and allowed to incubate with the calcite samples

273 for 1 hour. The calcite-saturated brine was used to prevent etch pit formation and to hydrate calcite

274 surface prior to adding IOS. Samples were then collected and dried following the procedure in

275 section 2.10. All calcite samples were prepared by cleaving on single crystal calcite.

276 NEXAFS measurements were performed at beamline 12-ID at the National Synchrotron Light

277 Source (NSLS-II). Fluorescence-yield (FY) NEXAFS data were collected near the sulfur K-edge

278 (2449-2504 eV) and calcium K-edge (4030-4110 eV) using a Pilatus 300 KW detector positioned

279 at 0.7° from the sample plane for both sulfur K-edge and calcium K-edge measurements. The total

280 intensity from a region of the detector away from any scattering peaks was used as a fluorescence

281 signal. Pre-edge subtraction and post-edge normalization was performed in Larch [56].

282 Subsequently, normalized spectra were decomposed using multipeak fitting package 2 in Igor pro

283 (WaveMetrics). Each spectrum was decomposed into 5 or less Gaussian functions and an

284 arctangent function following the approach proposed by Manceau and Nagy [57].

285 **2.11 Geochemical Modeling**

286 Geochemical modeling was performed using PHREEQC. The *phreeqc.dat* database was used

287 for thermodynamic data [58]. A list of reactions considered is in Table S1 (Supporting

288 Information). The model was run by first defining the composition of brine in equilibrium with

289 atmospheric CO_2 at 22 °C, and then equilibrating that solution with calcite and other Ca bearing

290 minerals in the Eagle Ford shale (i.e., dolomite, gypsum). The moles of added minerals and the

291 volume of solution were specified based on measured solution species and experimental conditions.

292 Additional details are in section 3.3.

293 **2.12 Density Functional Theory Calculations**

Density Functional Theory (DFT) calculations based on the Generalized Gradient Approximation (GGA) were performed using the Vienna Ab initio Simulation Package (VASP). A plane wave basis set was used with an energy cutoff of 300 eV and a Gaussian smearing at the Fermi level with a width of 0.05 eV to improve convergence. The Perdew-Burke-Ernzerhof (PBE) [64] functional was used to describe electron exchange and correlation. The Brillouin zone was sampled at the Γ-point. The convergence criteria for electronic and geometric optimization were 10^{-6} eV and 0.01 eV/Å, respectively.

To mimic the experimental surfaces, slab models of calcite $\{10\bar{1}4\}$ were constructed with the atoms in the bottom layer fixed in bulk positions. The thickness of the vacuum layer was set to 14 Å to isolate the periodic slabs. Our model of the IOS molecule had 10 carbon atoms in the hydrocarbon side chains. The binding energy of the IOS molecule to the calcite substrate was calculated as

$$E_{binding} = E_{surface-IOS} - E_{surface} - E_{IOS} \qquad (2)$$

where $E_{surface}$ is the energy of the calcite surface, E_{IOS} is the energy of isolated IOS molecule and $E_{surface-IOS}$ is the energy of the system when IOS binds to the calcite surface. The VASPsol code [65] was used to consider (implicit) solvent interactions as a continuum dielectric with a relative permittivity set to 78.4 to mimic water.

3. Results and Discussion

3.1 Sample Characterization Results

The measured SSA of Eagle Ford shale is 6.65±0.05 m^2/g. These results are consistent with SSA measurements in the literature for Eagle Ford shale [7]. Mineralogical results for our Eagle Ford shale are shown in Table 1. They show that the sample is comprised of 67% calcite, 8.7% quartz, 6.2% Illite and Mica, 4.2% Illite/Smectite mixture, 5% K-feldspar, 4.1% plagioclase, and minor amounts of pyrite, kaolinite, chlorite, apatite, and siderite. This composition is similar to that measured by others [6–8], except for the lack of small amounts of gypsum and dolomite.

The cation exchange capacity of the Eagle Ford shale is 89.1 meq/kg. The Ca and alkalinity (HCO$_3^-$) released into brine by Eagle Ford shale upon exposure to 0.5 M MgCl$_2$ after rinsing three times in brine were also measured. The difference between measured Ca and alkalinity was less than 0.01 mM. This indicates that at the start of Eagle Ford shale dissolution experiments (next

325   section) there was no Ca^{2+} available for release from cation exchange sites. Any Ca^{2+} initially
326   present at these sites was exchanged and removed during the triplicate KCl rinsing steps. Therefore,
327   any Ca^{2+} released during Eagle Ford shale dissolution experiments is likely due to mineral
328   dissolution.

329   Surface tension and contact angle results for calcite sample are presented in Table 2. The
330   surface tension decreases when IOS is added to the brine, and there is no difference for the two
331   IOS concentrations (which are both above the critical micelle concentration (CMC) of 94 mg/L).
332   Contact angles on freshly cleaved calcite decrease with IOS addition to brine. The same
333   measurements were taken on calcite after it was aged 12 hours in brine to create etch pits, and
334   contact angles were lower for all cases. Calcite-brine interfacial tension values were calculated
335   from Young's equation [60]; similar values were obtained for all setups (438 mJ/m^2 to 443 mJ/m^2)
336   except a lower value was obtained for aged calcite with brine only (411 mJ/m^2) By comparison,
337   Costa and Aquilano determined a comparable value of 409 mJ/m^2 for calcite and fresh water [55].
338   Aging calcite increases surface roughness (Section 3.5), which can further decrease interfacial
339   tension [61,62]. Costa and Aquilano allowed their sample to "equilibrate in air", which may have
340   increased surface roughness. Surface pressures (F) at the calcite-brine interface resulting from IOS
341   addition were calculated from differences in interfacial tension ($F = \gamma_{SL(IOSBrine),i} - \gamma_{SL(Brine),i}$,
342   where i is for fresh or aged calcite) following Fowkes and Harkins [63]. Values for fresh calcite
343   were very small and not distinguishable from zero, while values for aged calcite were relatively
344   large; the results indicate that the IOS preferentially adsorbs on aged versus fresh calcite-water
345   interfaces.

346   **3.2 Dissolution of Eagle Ford Shale**

347   Dissolution experiments were performed for Eagle Ford shale over a 48-hour period in brine
348   and IOS brine. Results for the first 12 hours are shown in Figure 2, and for the entire 48 hours
349   period in Figure S1 (Supporting Information). At the two IOS concentrations used (i.e., 500 and
350   3000 mg/L), approximately 61% (6.1 mg/g) and 12% (6.9 mg/g) of the IOS masses added to
351   solution adsorbed to shale components, respectively, based on measured adsorption isotherms [59].
352   Total surface area covered by adsorbed molecules was estimated using the minimum surface area
353   per molecule calculated from the Gibbs equation [64], i.e., 20.7 Å^2. Detailed calculations are in
354   the Supporting Information. The total surface area covered by IOS at 500 and 3000 mg/L are 34.6%
355   and 39.0% of the measured surface areas using N$_2$ adsorption, respectively. Also, IOS

356　concentrations in solutions (i.e., 194 mg/L and 2655 mg/L) after sorption at both loadings exceed

357　the CMC (94 mg/L). The elements Ca, Mg, Fe, S, Al, and Si were initially monitored in solution,

358　and only Ca, Mg, and S appreciably changed. For S, the sulfate ion (SO_4^{2-}) was measured using

359　ion chromatography and is reported in this form.

360　　Per Figure 2, the concentrations of Ca, Mg, and SO_4^{2-} all increased during the monitoring

361　period, and an initial rapid rise is followed by a decreasing rate of increase; the pH during this time

362　increases from 6.3 to approximately 8.0. This initial high rate of dissolution is expected, as fresh

363　brine solution contains very few mineral species (e.g., no Ca, Mg, SO_4^{2-}, and only low CO_3^{2-}) and

364　the driving force for dissolution is large. Over time, these species build up and mineral dissolution

365　slows, but does not appear to reach steady state after 48 hours. The Ca concentrations at 48 hours

366　are approximately 15 to 41 times greater than the SO_4^{2-} or Mg concentrations, respectively. Per

367　XRD, the only Ca containing mineral measured was calcite. However, the presence of Mg and

368　SO_4^{2-} indicates minor amounts of dolomite and gypsum are present, and they have been identified

369　in other samples of Eagle Ford shale [6–8].

370　　Also per Figure 2, Ca, Mg, and SO_4^{2-} concentrations in brine and IOS brine are different. For

371　Ca, this difference is only significant at 3 hours, and then it becomes indistinguishable with respect

372　to the measurement error. However, for Mg and SO_4^{2-} the differences persist over 48 hours, but

373　the magnitudes of these differences are small compared to those for Ca at 3 hours. Results for the

374　different IOS concentrations are not as consistent. For example, less Ca dissolves for IOS 500

375　compared to IOS 3000, whereas for SO_4^{2-} the opposite is true. The reason for the conflicting trends

376　is not clear, and may be due to transient uptake of IOS and/or inorganic ions onto ion exchange

377　sites and/or hydrophobic domains in organic matter. Regardless, these results indicate that IOS

378　protects shale minerals from dissolution. They also indicate that IOS primarily protects calcite

379　from dissolution in the Eagle Ford shale but this effect is transient.

380　　The pH and total carbonate were monitored during Eagle Ford shale dissolution and (along

381　with ionic strength) used to calculated ion activities, (i.e., a_{H^+}, $a_{H_2CO_3^*}$, a_{H_2O}, $a_{Ca^{2+}}$, $a_{HCO_3^-}$).

382　These were used with calculated rate constants from Plummer et al. [32] to approximate which

383　terms in equation 1 dominate calcite dissolution from the shale. At all times after time zero, $k_3 a_{H_2O}$

384　and $k_4 a_{Ca^{2+}} a_{HCO_3^-}$ dominate equation 1 (Table S3). At 3 hours, $k_3 a_{H_2O}$ slightly exceeds

385　$k_4 a_{Ca^{2+}} a_{HCO_3^-}$; after this time the opposite occurs, indicating precipitation is possible. However,

386 the saturation index (SI) for calcite remains below 0 at all times, indicating only dissolution and
387 not precipitation is active.

3.3 Ca^{2+} Mass Balance in Eagle Ford Shale

389   PHREEQC modeling was performed to determine if the Ca measured in brine solution during
390 Eagle Ford shale dissolution at 48 hours was near equilibrium with calcite, and/or if other
391 unaccounted sources of Ca were present. Modeling results are presented in Figure 2d; model
392 equations are presented in Table S1 (Supporting Information). Only minerals containing Ca, Mg,
393 CO_3^{2-}, and SO_4^{2-} were considered, since only these were identified in brine. Three different mineral
394 phases were defined in modeling. Calcite was defined as an infinite mineral, since 67.5% of Eagle
395 Ford shale is calcite. Dolomite and gypsum were also considered sources of Ca, and the moles of
396 these minerals were set equal to the moles of Mg and SO_4^{2-} in solution at 48 hours, respectively.
397 Alkalinity and pH were measured at 48 hours and were used to determine pCO_2. Finally, modeled
398 pH, alkalinity, Mg, and SO_4^{2-} were compared with measured values for validation. The measured
399 Ca concentration in solution after 48 hours represents the baseline for comparison.

400   Results in Figure 2d show that the measured Ca in solution is approximately 95.5% of the
401 theoretical value at equilibrium. The contributions from dolomite and gypsum to modeled total Ca
402 are 2.2% and 6.6% of total Ca, respectively, with the remaining contribution (91.2%) from calcite.
403 Aqueous Ca complexes corresponding to three different modeling cases in Figure 2d are presented
404 in Table S2. Speciation results for the case considering all three minerals (calcite, dolomite, and
405 gypsum) show that the effect of $CaSO_4(aq)$, which can affect the free Ca^{2+} concentration, is
406 negligible. Hence, PHREEQC model results show that (as expected) calcite is the major
407 contributor of Ca in solution, and they uniquely suggest that IOS is primarily suppressing Ca
408 release from this mineral at 3 hours. For this reason, the mechanisms of IOS inhibition on calcite
409 were identified for further study.

3.4 Dissolution of Calcite

411   The effects of 500 and 3000 mg/L IOS addition to brine on calcite dissolution were evaluated
412 over 36 hours using sieved calcite particles (150-850 μm); results are shown in Figure 3a. As with
413 Eagle Ford shale, Ca concentrations in brine with only calcite increase during the monitoring
414 period, and an initial rapid rise is followed by a decreasing rate of increase. This is expected
415 because calcite constituent concentrations (i.e., Ca and CO_3^{2-}) in brine are initially very low, and
416 they increase over time. Comparison of Ca concentrations in brine and IOS brine shows that IOS

417 inhibits dissolution of the calcite particles, although differences at 1 and 36 hours are not
418 significant (Figure 3a).

419 Results from the calcite particles motivated similar measurements on cleaved calcite at 12
420 hours, but over a wider concentration range; results are shown in Figure 3b. Measured
421 concentrations of Ca decrease with increasing concentration of IOS from 1 mg/L to 50 mg/L (by
422 up to 90% compared to brine only), and then increase as the IOS concentration exceeds the CMC
423 (94 mg/L). The results show for the first time that a surfactant can substantially inhibit calcite
424 dissolution, and that this inhibition is greatest at intermediate surfactant concentrations. Percent
425 surface coverage at each concentration was calculated based on the same approach taken to
426 calculate surface area coverage for Eagle Ford shale (Section 3.2), and values at 1, 10, 50, 500 and
427 3000 mg/L of IOS are 1.10, 9.78, 32.78, 69.66 and 77.76%, respectively. Interestingly, the
428 minimum area per molecule calculated from the Gibbs equation (20.7 Å^2) is in good agreement
429 with that calculated solely from the adsorption isotherm assuming bilayer adsorption (26.2 Å^2).
430 Surface coverage calculations using either the minimum area per molecule from the Gibbs
431 equation or the adsorption isotherm predict monolayer coverage is not exceeded, so results
432 showing less inhibition above 50 mg/L were not expected.

433 The results suggest that above the CMC (i.e., 94 mg/L), the adsorption density decreases with
434 increasing concentration and thus less inhibition occurs. This might be due to aggregation of IOS
435 above the CMC. Several prior works evaluated surfactant sorption using AFM or molecular
436 dynamics; they demonstrated that surfactants do not always form a continuous film (i.e.,
437 monolayer or bilayer). That can aggregate to form micelles, hemimicelles and/or rodlike
438 aggregates on various surfaces at elevated concentrations [65–68]. We also determined via AFM
439 that IOS can form micelles or hemimicelles on a calcite surface at 1000 mg/L (10xCMC). Thus,
440 decreasing adsorption density of IOS with increasing concentration above the CMC appears
441 reasonable.

442 The pH and total carbonate concentration were also monitored during calcite dissolution and
443 (along with ionic strength) used to calculate ion activities, (i.e., a_{H^+}, $a_{H_2CO_3^*}$, a_{H_2O}, $a_{Ca^{2+}}$, $a_{HCO_3^-}$).
444 These were used with the aforementioned rate constants to determine which terms in equation 1
445 dominate dissolution [32]. At zero and 3 hours, $k_3 a_{H_2O}$ dominates (Table S4). For 6 hours and
446 greater, values of $k_3 a_{H_2O}$ are similar to or less than $k_4 a_{Ca^{2+}} a_{HCO_3^-}$, indicating precipitation is also
447 possible. The saturation index ($SI = \log{(Q/K_{sp})}$) was also calculated at each time point. It is

448 negative up to and including 6 hours, and equal to only 0.06 and 0.21 at 12 and 36 hours,

449 respectively. Hence, precipitation is less likely until greater than 36 hours.

450   PHREEQC modeling was also performed to determine if the Ca measured in brine solutions

451 during calcite dissolution was near equilibrium. The simulated equilibrium value is approximately

452 1 mM (Figure 3b, blue bar). The simulated value is similar to the calcium concentration with

453 cleaved calcite at 12 hours (0.95 mM), but below that for calcite particles at 36 hours (1.4 mM).

454 The calcite particles after 36 hours are likely closer to equilibrium; the reason that the equilibrium

455 Ca value is below the measured value may be due to a small error in the final pH measurement.

456 An error of 0.1 near pH 8 will result in a modeled Ca concentration that is 0.5 mM different.

457 **3.5 Calcite Etch Pit Progression and Morphology**

458   Laser profilometry was used to probe etch pit development and identify dissolution

459 mechanisms on freshly cleaved calcite surfaces (i.e., $\{10\bar{1}4\}$ face) placed in brine without and with

460 IOS for 12 hours. Results shown in Figure 4 provide spatial resolution that spans more than three

461 orders of magnitude. In brine only samples, relatively deep and large etch pits are created; etch pit

462 depths are on the order of 5 μm, and etch pit side lengths are approximately 100 μm (Figure 4a).

463 These etch pits vary in shape from classical rhombohedral to more triangular, where the latter are

464 truncated across the obtuse side of the rhombus along the [010] direction. In IOS brine by contrast,

465 only relatively shallow and small etch pits are created, with depths less than 0.15 μm; also, these

466 etch pits are similar at the two IOS concentrations. Etch pits side lengths are less than 40 μm

467 (Figure 4b and 4c). Hence, IOS addition to brine does not prevent initial dissolution but does

468 appear to inhibit etch pit growth.

469   Cross-sectional profiles across etch pits are also shown in Figure 4. Etch pit angles were

470 calculated, and are noted in Table 3. In the presence of only brine, the etch pit angle is smaller on

471 the acute side of each rhombus, indicating that pit growth is faster on this edge. This is consistent

472 with faster pit growth at this edge observed in the presence of Mg^{2+} by Arvidson et al. [33]. In the

473 presence of pure water, others observed faster etch pit growth along obtuse edges [69]. In the

474 presence of IOS brine, the shallow and small etch pits formed give rise to very small angles.

475   Etch pit densities were calculated (i.e., etch pit area divided by total area), and results are

476 presented in Figure 5b. Surprisingly, a higher fraction of the calcite surface is covered with etch

477 pits for calcite samples in IOS brine compared to only brine. This is also apparent by comparing

478 Figure 4a with either Figure 4b or 4c. These results indicate a contrasting effect, namely that IOS

479 promotes etch pit formation but restricts etch pit growth. These contrasting observations are

480 possible because of the large spatial scale (0.05 to 200 μm) spanned by laser profilometry.

481   In a second set of experiments, calcite surfaces reacted in only brine for 12 hours and then

482 dried were re-submerged in either brine or IOS brine for another 12 hours. Results are shown in

483 Figure 6. As expected, etch pits submerged in only brine for the second 12 hours continued to

484 grow, and in some cases coalesced. However, etch pits submerged in IOS brine for the second 12

485 hours were almost completely arrested, i.e., they do not appear to have grown further. Examination

486 of the line profiles drawn through etch pits grown in only brine the second 12 hours shows that the

487 majority of etch pit growth was along the acute side of each rhombus (blue area in Figure 6), again

488 indicating preferential growth on this edge.

489   A surprising result from Figure 6 is that additional etch pits were not initiated when the sample

490 initially aged in brine only was then aged for another 12 hours in IOS brine. From Figure 4, it is

491 apparent that very high etch pit densities occur when freshly cleaved calcite is initially placed into

492 IOS brine. It is possible that initially formed μm-deep etch pits dominated surfactant sorption and

493 reduce its concentration on flat $\{10\bar{1}4\}$ surfaces, thereby reducing the initiation of new etch pits.

494 **3.6 Preferential Adsorption of IOS on Calcite Etch Pits**

495   ToF-SIMS 2D(XY) profiles of SO_2^- for a control sample (calcite aged in brine) and samples

496 aged in 10 or 100 mg/L IOS (calcite aged in brine and then incubated in IOS) are shown in Figure

497 8. The depth profile of SO_2^- in Figure 7 confirms that with IOS adsorption, SO_2^- accumulates on

498 the top surface of calcite. When no IOS is added to brine, then SO_2^- is not detected on the sample

499 surface (Figure 8a). At 10 mg/L (0.1xCMC), IOS appears to preferentially adsorb at acuate edges,

500 with distinct areas of high (yellow) and low (brown) coverage (Figure 8b). While at 100 mg/L,

501 when the concentration is near the CMC, IOS coverage on the surface appears more uniform with

502 intermediate (orange) coverage (Figure 8c). Preferential IOS adsorption at 10 mg/L to acute edges

503 versus obtuse edges and terrace sites is facilitated by comparison of Figure 8b to Figure 8d, where

504 in the latter the terrace, acute edge, and obtuse edge sites are color coded from the laser

505 profilometry image for ease of comparison. Interestingly, surface coverage on the acute edges

506 appears to be denser than that on the terrace and obtuse edges. Less dense coverage on the obtuse

507 edge might be due a lower step density at obtuse edges compared to acute edges. A conceptual

508 model of the surface profile along the line indicated by the double arrow in Figure 8d is presented

509 in Figure 8e. It is based on the observation that the obtuse edge is much steeper than the acute edge,

510   such that the latter has more steps that preferentially adsorb IOS. This gives rise to more IOS

511   adsorption on the acute versus the obtuse sides of the pit.

512   Sulfur K-edge NEXAFS spectra of two calibrants (IOS and Gypsum), one control, and four

513   experimental cases are shown in Figure 9. By decomposing the calibrants (Figure 9a-b), the

514   energies of the s $\rightarrow$ p electron transitions of sulfonate and sulfate groups were identified and are

515   approximately 2481($G_{sulfonate}$) and 2482.5 ($G_{sulfate}$) eV, respectively; these are in good agreement

516   with reported values [57]. In addition, sulfate impurities in IOS were also identified ($G_{sulfate, IOS}$).

517   Since optical quality calcite crystals used in this study originated from nature, sulfur impurities

518   (i.e., sulfite, sulfonate, and sulfate) were observed in all samples (Figure 9c-e). The fractional

519   contributions of three different sulfur functional groups ($G_{sulfite, Impr}$, $G_{sulfonate, Impr}$, and $G_{sulfate, Impr}$)

520   to the measured peaks were calculated based on the area of Gaussian functions as shown in Figure

521   9c. To distinguish the contributions of IOS to sulfonate (2481 eV) and sulfate (2482.5 eV), two

522   Gaussian functions (e.g., $G_{sulfonate, IOS}$ (red line) and $G_{sulfonate, Impr}$ (blue line)) were used to

523   decompose each functional group contribution. The ratio between impurities was fixed, assuming

524   that ratios of sulfite to sulfonate and sulfite to sulfate for all calcite samples are identical.

525   Ultimately, areas of $G_{sulfonate, IOS}$ (green) in Figure 9d-g were calculated and summarized in Figure

526   9h. Detailed Gaussian-Arctan fitting parameters are in Table S5.

527   Decomposed NEXASF spectra for each of the IOS adsorbed calcite samples are in good

528   agreement with findings in ToF-SIMS results. The existence of $G_{sulfonate, IOS}$, and differences in

529   areas between samples, indicate that SO_2^- detected by ToF-SIMS originates from adsorbed IOS on

530   calcite surfaces. The decomposed NEXAFS spectra enable semiquantitative comparison of the

531   amount of IOS adsorbed on calcite surfaces. Overall, amounts of IOS adsorbed on etched calcite

532   samples were greater than those on unetched (i.e., Not Etched) samples. In agreement with ToF-

533   SIMS results, the NEXASF spectra indicate that IOS preferentially adsorb more to edges compared

534   to terraces on calcite surfaces. Moreover, when samples were exposed to higher concentration of

535   IOS, greater amounts of IOS partitioned onto calcite surfaces (i.e., Figure 9h Etched 10 vs Etched

536   100), as observed with ToF-SIMS (Figure 8a-c),

537   Calcium K-edge NEXAFS spectra were also measured to probe the effect of IOS adsorption

538   to Ca bonding environment and formation of polymorphs of calcium carbonate. No substantial

539   difference in Ca K-edge NEXAFS spectra were observed between samples (Figure S2). This might

540   be due to broad spectra peaks or a suppression of shifted surface Ca peaks by large bulk calcite

541   peaks. Meanwhile, polymorphs of $CaCO_3$ can form under different thermodynamic conditions and

542   in the presence of surfactants. For example, Chen and Nan reported that precipitation of $CaCO_3$

543   polymorphs such as aragonite and vaterite can occur in the presence of anionic surfactants [70].

544   However, as shown in Figure S2, obtained Ca K-edge NEXAFS spectra of four samples and

545   pristine calcite were similar to the reference calcite spectrum, and characteristic peaks of $CaCO_3$

546   polymorphs (i.e., amorphous calcium carbonate (ACC), aragonite and vaterite) are not apparent.

547   Prior efforts to identify preferential adsorption of solutes on edge or terrace sites have relied

548   on less direct measures. Walker et al. treated cleaved calcite with a nonionic surfactant,

549   hexamethyldisilazane (HMDS), to alter calcite wettability. They used Kelvin probe force

550   microscopy (KPFM) to indicate preferential HMDS adsorption at existing step or edge sites [24].

551   Elhadj et al. and Sand et al. used AFM to image acute and obtuse step edge morphology changes

552   during precipitation in the absence and presence of polyaspartic acid and polysaccharides,

553   respectively [43,71]. They inferred binding location from these measurements, and supported their

554   interpretation with theoretical binding energy calculations. The ToF-SIMS and sulfur K-edge

555   NEXAFS results in this study provide direct evidence of preferential IOS adsorption at acute edge

556   sites, thereby suggesting adsorbed IOS is inhibiting dissolution via step pinning at these locations.

557   **3.7 DFT Simulation of IOS Adsorption on Calcite Surfaces**

558   In order to better understand the experimental results, DFT was used to calculate binding

559   energies of the IOS molecule on the calcite surface, and binding geometries of the IOS molecule

560   at terrace, acute and obtuse step sites are shown in Figure 10. The calculated binding energies are

561   shown in Table 4. Our most accurate calculations with implicit solvation indicate that IOS binding

562   is strongest at the acute step (-1.02 eV) site followed closely by the obtuse step (-0.94 eV), and

563   binding at the terrace site (-0.27 eV) is weakest. The same trend was observed for both vacuum

564   and our implicit solvent model, as shown in Table 4. These calculations help to explain how

565   preferential IOS adsorption at both acute and obtuse sites can disrupt and inhibit calcite dissolution.

566   They also support the preferential adsorption of IOS at acuate versus obtuse sites as indicated by

567   ToF-SIMS in subsection 3.6, and indicate this is at least partially due to preferential adsorption at

568   acute edge versus obtuse edge sites.

569   **3.8 Discussion**

570   Results in this work highlight two apparently opposite effects of the IOS on calcite dissolution.

571   The first is the formation of more etch pits (i.e., higher density) in the presence of IOS (e.g., 12

572   hours, Figure 3b), and the second is the inhibition of etch pit growth by IOS once they are created.

573   Miyata et al. used molecular dynamics to interrogate mechanisms responsible for the growth of

574   etch pits [72]. They simulated dissolution at a calcite edge site, and determined that dissolution

575   starts when adsorbed water dissociates, and the proton is transferred to CO_3 and the hydroxyl ion

576   to Ca. This allows bonds between the proton stabilized CO_3 and Ca to break, creating a separate

577   bicarbonate ion (HCO_3^-) that desorbs from the calcite edge. The HCO_3^- then decomposes to a

578   hydroxide ion and CO_2, the hydroxide ion adsorbs to Ca, and adsorbed $Ca(OH)_2$ is formed which

579   can desorb into solution. The CO_2 released into solution then forms bicarbonate in bulk water at

580   circumneutral pH. That study highlights the importance of adsorbed water in facilitating Ca and

581   CO_3 hydration at the calcite surface and indicates that solutes that disrupt adsorbed water will

582   affect calcite dissolution.

583   Nada and Shen et al. determined the binding conformation of aspartic acid and polystyrene

584   sulfonate on a calcite $\{10\bar{1}4\}$ surface using molecular dynamics [48,73]. First, they showed that

585   three layers of structured water molecules form on the calcite $\{10\bar{1}4\}$ surface. Adsorbed aspartic

586   acid and polystyrene sulfonate are separated from calcite $\{10\bar{1}4\}$ surface by one or two intervening

587   structured water molecules, and form a weak nonspecific bond with calcite $\{10\bar{1}4\}$ surface. In

588   addition, Elhadj et al. studied the effect of polyaspartic acid concentration and chain length on

589   calcite crystal growth, and observed growth enhancement at low concentrations and a transition to

590   growth inhibition at high concentrations, where the transition occurred at lower concentrations for

591   larger polyaspatic acids [43]. They attribute the transition to the number of calcite edge sites where

592   polyaspartic acids displace water molecules. At low polyaspartic acid concentrations and low

593   water displacement, sufficient restructuring of water occurs at the calcite surface to reduce the

594   energy for diffusion of solvated ions across this boundary [44]. However, at high polyapsartic acid

595   concentrations and high water displacement, there is sufficient dehydration of contiguous water

596   molecules at the surface that solvation of Ca and CO_3 is inhibited. It follows that the strength

597   and/or amount of IOS adsorption on flat versus edge sites may control contrasting patterns of rapid

598   initial pit formation versus slow pit growth during dissolution.

599   Surface pressure values calculated from interfacial tensions (Table 2) indicate preferential IOS

600   adsorption to etched versus smooth calcite surfaces, where the former have a higher density of

601   edge sites. ToF-SIMS and sulfur K-edge NEXAFS results support this interpretation, and show

602   IOS preferentially adsorbs to acute versus obtuse and terrace sites. Our DFT results also support

19

preferential IOS adsorption at acute sites, which is only slightly more favorable than adsorption at obtuse sites, and much more favorable than adsorption at terrace sites (i.e., by 0.60-1.66 eV). Similarly, Elhadj et al. found that polyaspartic acids adsorb more strongly to calcite edge versus terrace (flat) sites (by 1.3-6.5 eV) [43]. This leads us to postulate a conceptual model, where oxygen in the sulfonate head group of IOS interacts with Ca at calcite surfaces and displaces water. On calcite terraces, weaker adsorption energies indicates that fewer adsorbed IOS molecules per area displace less water, and they are characterized by faster attachment and detachment rates compared to edge sites. This disruption of water at flat surfaces could lower the energy barrier for diffusion of solvated molecules across the water hydration layer and promote faster pit formation (relative to brine only). However, at edge sites, where more strongly adsorbed IOS molecules are present, IOS molecules displace many more water molecules, and this inhibits CO_3 and Ca solvation and retards pit growth. Our calcite dissolution results with varying IOS concentrations show that as IOS concentrations exceed the CMC calcite dissolution rates increase, and this appears to be caused by IOS aggregation into micelles or hemimicelles on the calcite surface that reduces edge site adsorption coverage.

Surface complexation models (SCMs) for carbonates have been used to explain adsorption isotherms, surface charge, and to model dissolution and growth kinetics when inhibitors are present [74–78]. Defining reactions of surface species and their concentrations significantly affects the accuracy of modeling results. For example, Tagavifar et al. used the diffusion layer model (DLM), which assumes formation of inner sphere complexes, to model surfactant binding to a limestone surface without intervening water molecules [76]. They suggested two different surface reactions were needed based on the surfactant chemical structure: strong adsorption by charge regulated complexation with the surfactant head group; weak adsorption by hydrogen bonding between ethoxy or propoxy groups in the hydrocarbon chain. These proposed complexation reactions were not supported by spectroscopic or computational (i.e., molecular dynamics and DFT) evidence. However, binding energies from our DFT efforts, as well as ToF-SIM and Sulfur K-edge NEXAFS results, support stronger inner sphere complexation of IOS at defect sites (i.e., acute and obtuse edges). They also support weaker complexation at terrace sites, and the exact conformation of IOS at these sites requires further study via DFT and/or spectroscopic evaluation.

4. Conclusions

634 Primary findings in this work are the following:

635 • Adsorption of IOS to surfaces of minerals in Eagle Ford shale kinetically inhibited overall
636   release of Ca into bulk solution, and this is attributed to inhibition dissolution of calcite
637   dissolution.

638 • IOS adsorption from brine to calcite both enhances initial etch pit formation, and prevents
639   further etch pit growth.

640 • ToF-SIMS, S K-edge NEXAFS and DFT results indicate that IOS preferentially adsorbs to
641   edge sites compared to terrace sites.

642 • The weak binding of IOS to terrace sites observed in this work suggests that enhanced etch pit
643   formation in IOS-containing brines is due to the disruption of structured water molecules at
644   flat surfaces by IOS, resulting in relatively lower energy barriers for diffusion of solvated ions
645   to and from the calcite surface.

646 • The strong preferential binding of IOS to edge sites suggests that inhibited etch pit growth in
647   IOS-containing brines is due to displacement of water molecules at defect sites (i.e., obtuse
648   and acute edges) by strongly adsorbed IOS molecules, resulting in limiting solvation of calcite.

649

650 This work shows for the first time how surfactant adsorption amount and location to calcite
651 surfaces can be probed over spatial scales approaching hundreds of microns using optical
652 profilometry coupled with ToF-SIMS and NEXAFS. By comparison, AFM measurements of
653 surfactant adsorption on calcite surfaces are limited to only a few microns. The implications of
654 these results are that surfactants added to slick water, foams, and carbon dioxide injected into shale
655 or conventional formations can inhibit dissolution of carbonate minerals. This may mitigate the
656 formation of preferential flow paths, that could enhance oil and gas recovery from shales, or serve
657 as conduits for upward fluid migration from deep reservoirs to potable groundwater. Further work
658 is needed to determine if the observed effects extend to reservoir pressures and temperatures, and
659 possible implications of these mechanisms in real reservoirs.

CRediT authorship contribution statement

Kyung Tae Kim: Conceptualization, Methodology, Software, Formal analysis, Investigation, Data Curation, Visualization, Writing - original draft. **Mantha Sai Pavan Jagannath:** Methodology, Software, Investigation, Visualization, Writing - original draft. **Gregory M. Su**: Methodology, Software, Investigation**,** Writing - review & editing **Guillaume Freychet:** Methodology, Investigation**,** Writing - review & editing. **Tongzhou Zeng:** Conceptualization, Methodology, Formal analysis, Investigation. **Kishore K. Mohanty:** Conceptualization, Methodology, Resources, Validation, Supervision, Funding acquisition, Writing - review & editing. **Graeme Henkelman:** Conceptualization, Validation, Supervision, Writing - review & editing. **Lynn E. Katz:** Conceptualization, Methodology, Validation, Supervision, Funding acquisition Writing - review & editing. **Charles J. Werth:** Conceptualization, Methodology, Validation, Supervision, Funding acquisition, Writing - original draft, Writing - review & editing, Project administration.

Declaration of Competing interest

The authors declare that they have no known competing financial interests or personal relationships that could have appeared to influence the work reported in this paper.

References

[1]   EIA, EIA/ARI world shale gas and shale oil resource assessment technically recoverable shale gas and shale oil resources: an assessment of 137 shale formations in 41 countries outside the United States, 2013. www.adv-res.com.

[2]   EIA, Annual energy outlook 2014 with projections to 2040, 2014. www.eia.gov/forecasts/aeo.

[3]   F. Liu, P. Lu, C. Griffith, S.W. Hedges, Y. Soong, H. Hellevang, C. Zhu, CO2-brine-caprock interaction: Reactivity experiments on Eau Claire shale and a review of relevant literature, Int. J. Greenh. Gas Control. 7 (2012) 153–167. https://doi.org/10.1016/j.ijggc.2012.01.012.

[4]   M.F. Irfan, T.M. Bisson, E. Bobicki, F. Arguelles-Vivas, Z. Xu, Q. Liu, T. Babadagli, CO2 storage in saline aquifers by dissolution and residual trapping under supercritical conditions: An experimental investigation, Colloids Surfaces A Physicochem. Eng. Asp. 548 (2018) 37–45. https://doi.org/10.1016/j.colsurfa.2018.03.062.

[5]   J.A. Chermak, M.E. Schreiber, Mineralogy and trace element geochemistry of gas shales in the United States: Environmental implications, Int. J. Coal Geol. 126 (2014) 32–44.

[6]   W.C. Dawson, Shale microfacies: Eagle Ford Group (Cenomanian-Turonian) north-central Texas outcrops and subsurface equivalents, Gulf Coast Assoc. Geol. Soc. Trans. 50 (2000) 607–621.

[7]   D.S. Jennings, J. Antia, W.K. Camp, E. Diaz, B. Wawak, Petrographic characterization of the Eagle Ford Shale, South Texas: Mineralogy, common constituents, and distribution of nanometer-scale pore types, Electron Microsc. Shale Hydrocarb. Reserv. AAPG Mem. 102 (2013) 101–113.

[8]   J. Schieber, R. Lazar, K. Bohacs, R. Klimentidis, M. Dumitrescu, J. Ottmann, An sem study of porosity in the eagle ford shale of Texas-pore types and porosity distribution in a depositional and sequence-stratigraphic context, AAPG Mem. 110 (2016) 167–186. https://doi.org/10.1306/13541961M1103589.

[9]   F. Gherardi, T. Xu, K. Pruess, Numerical modeling of self-limiting and self-enhancing caprock alteration induced by CO2 storage in a depleted gas reservoir, Chem. Geol. 244 (2007) 103–129.

[10]   R. Lahann, M. Mastalerz, J.A. Rupp, A. Drobniak, Influence of CO2 on New Albany

720   Shale composition and pore structure, Int. J. Coal Geol. 108 (2013) 2–9.

721   [11]   J. Rohmer, A. Pluymakers, F. Renard, Mechano-chemical interactions in sedimentary

722   rocks in the context of CO2 storage: Weak acid, weak effects?, Earth-Science Rev. 157

723   (2016) 86–110. https://doi.org/10.1016/j.earscirev.2016.03.009.

724   [12]   J.P. Verdon, Significance for secure CO2 storage of earthquakes induced by fluid

725   injection, Environ. Res. Lett. 9 (2014) 1–10. https://doi.org/10.1088/1748-

726   9326/9/6/064022.

727   [13]   S.A. Carroll, W.W. Mcnab, Z. Dai, S.C. Torres, Reactivity of Mount Simon Sandstone

728   and the Eau Claire Shale Under CO2 Storage Conditions, Environ. Sci. Technol. 47

729   (2013) 252–261. https://doi.org/10.1021/es301269k.

730   [14]   V. Marcon, C. Joseph, K.E. Carter, S.W. Hedges, C.L. Lopano, G.D. Guthrie, J.A. Hakala,

731   Experimental insights into geochemical changes in hydraulically fractured Marcellus

732   Shale, Appl. Geochemistry. 76 (2017) 36–50.

733   [15]   A.N. Paukert Vankeuren, J.A. Hakala, K. Jarvis, J.E. Moore, Mineral Reactions in Shale

734   Gas Reservoirs: Barite Scale Formation from Reusing Produced Water As Hydraulic

735   Fracturing Fluid, Environ. Sci. Technol. 51 (2017) 9391–9402.

736   https://doi.org/10.1021/acs.est.7b01979.

737   [16]   J.J. Sheng, Status of surfactant EOR technology, Petroleum. 1 (2015) 97–105.

738   https://doi.org/10.1016/j.petlm.2015.07.003.

739   [17]   H.C. Tamayo, K.J. Lee, R.S. Taylor, Enhanced aqueous fracturing fluid recovery from

740   tight gas formations: Foamed CO2 pre-pad fracturing fluid and more effective surfactant

741   systems, J. Can. Pet. Technol. 47 (2008) 33–38. https://doi.org/10.2118/08-10-33.

742   [18]   C. Negin, S. Ali, Q. Xie, Most common surfactants employed in chemical enhanced oil

743   recovery, Petroleum. 3 (2017) 197–211. https://doi.org/10.1016/j.petlm.2016.11.007.

744   [19]   S. Paria, K.C. Khilar, A review on experimental studies of surfactant adsorption at the

745   hydrophilic solid-water interface, Adv. Colloid Interface Sci. 110 (2004) 75–95.

746   https://doi.org/10.1016/j.cis.2004.03.001.

747   [20]   B. Li, E. Ruckenstein, Adsorption of ionic surfactants on charged solid surfaces from

748   aqueous solutions, Langmuir. 12 (1996) 5052–5063.

749   [21]   P. Somasundaran, G.E. Agar, The zero point of charge of calcite, J. Colloid Interface Sci.

750   24 (1967) 433–440. https://doi.org/10.1016/0021-9797(67)90241-X.

751   [22]   T. Ahmadall, M. V Gonzalez, J.H. Harwell, J.F. Scamehorn, Reducing Surfactant

752   Adsorption in Carbonate Reservoirs, SPE Reserv. Eng. 8 (1993) 117–122.

753   https://doi.org/10.2118/24105-PA.

754   [23]   J.F. Scamehorn, R.S. Schechter, W.H. Wade, Adsorption of surfactants on mineral oxide

755   surfaces from aqueous solutions. I: Isomerically pure anionic surfactants, J. Colloid

756   Interface Sci. 85 (1982) 463–478. https://doi.org/10.1016/0021-9797(82)90013-3.

757   [24]   S.M. Walker, M.C. Marcano, S. Kim, S.D. Taylor, U. Becker, Understanding Calcite

758   Wettability Alteration through Surface Potential Measurements and Molecular

759   Simulations, J. Phys. Chem. C. 121 (2017) 28017–28030.

760   https://doi.org/10.1021/acs.jpcc.7b09565.

761   [25]   H.M. Abd El-Lateef, V.M. Abbasov, L.I. Aliyeva, E.E. Qasimov, I.T. Ismayilov,

762   Inhibition of carbon steel corrosion in CO2-saturated brine using some newly surfactants

763   based on palm oil: Experimental and theoretical investigations, Mater. Chem. Phys. 142

764   (2013) 502–512. https://doi.org/10.1016/j.matchemphys.2013.07.044.

765   [26]   U. Wehrmeister, D.E. Jacob, A.L. Soldati, N. Loges, T. Häger, W. Hofmeister,

766   Amorphous, nanocrystalline and crystalline calcium carbonates in biological materials, J.

767   Raman Spectrosc. 42 (2011) 926–935. https://doi.org/10.1002/jrs.2835.

768   [27]   T. Matschei, B. Lothenbach, F.P. Glasser, The role of calcium carbonate in cement

769   hydration, Cem. Concr. Res. 37 (2007) 551–558.

770   https://doi.org/10.1016/j.cemconres.2006.10.013.

771   [28]   N.H. De Leeuw, S.C. Parker, J.H. Harding, Molecular dynamics simulation of crystal

772   dissolution from calcite steps, Phys. Rev. B. 60 (1999) 13792.

773   [29]   I.N. MacInnis, S.L. Brantley, The role of dislocations and surface morphology in calcite

774   dissolution, Geochim. Cosmochim. Acta. 56 (1992) 1113–1126.

775   https://doi.org/10.1016/0016-7037(92)90049-O.

776   [30]   C.A. Orme, A. Noy, A. Wierzbicki, M.T. Mcbride, M. Grantham, H.H. Teng, P.M. Dove,

777   J.J. Deyoreo, Formation of chiral morphologies through selective binding of amino acids

778   to calcite surface steps, Nature. 411 (2001) 775–779. https://doi.org/10.1038/35081034.

779   [31]   W. Stumm, Reactivity at the mineral-water interface: Dissolution and inhibition, Colloids

780   Surfaces A Physicochem. Eng. Asp. 120 (1997) 143–166. https://doi.org/10.1016/S0927-

781   7757(96)03866-6.

782   [32]   L.N. Plummer, Wigley T. M. L., D.L. Parkhurst, The Kinetics of Calcite Dissolution In
783   CO2-Water systems at 5 degrees to 60 degrees C and 0.0 to 1.0 atm CO2, Am. J. Sci. 278
784   (1978) 179–216. https://doi.org/10.2475/ajs.278.2.179.

785   [33]   R.S. Arvidson, M. Collier, K.J. Davis, M.D. Vinson, J.E. Amonette, A. Luttge,
786   Magnesium inhibition of calcite dissolution kinetics, Geochim. Cosmochim. Acta. 70
787   (2006) 583–594.

788   [34]   D.W. Britt, V. Hlady, In-situ atomic force microscope imaging of calcite etch pit
789   morphology changes in undersaturated and 1-hydroxyethylidene-1, 1-diphosphonic acid
790   poisoned solutions, Langmuir. 13 (1997) 1873–1876.

791   [35]   R.G. Compton, C.A. Brown, The inhibition of calcite dissolution/precipitation: 1, 2-
792   dicarboxylic acids, J. Colloid Interface Sci. 170 (1995) 586–590.

793   [36]   N.H. De Leeuw, Molecular dynamics simulations of the growth inhibiting effect of Fe2+,
794   Mg2+, Cd2+, and Sr2+ on calcite crystal growth, J. Phys. Chem. B. 106 (2002) 5241–
795   5249.

796   [37]   P.M. Dove, M.F. Hochella Jr, Calcite precipitation mechanisms and inhibition by
797   orthophosphate: In situ observations by Scanning Force Microscopy, Geochim.
798   Cosmochim. Acta. 57 (1993) 705–714.

799   [38]   C.N. Fredd, H.S. Fogler, The influence of chelating agents on the kinetics of calcite
800   dissolution, J. Colloid Interface Sci. 204 (1998) 187–197.

801   [39]   A.R. Hoch, M.M. Reddy, G.R. Aiken, Calcite crystal growth inhibition by humic
802   substances with emphasis on hydrophobic acids from the Florida Everglades, Geochim.
803   Cosmochim. Acta. 64 (2000) 61–72.

804   [40]   M. Ricci, J.J. Segura, B.W. Erickson, G. Fantner, F. Stellacci, K. Voïtchovsky, Growth
805   and Dissolution of Calcite in the Presence of Adsorbed Stearic Acid, Langmuir. 31 (2015)
806   7563–7571. https://doi.org/10.1021/acs.langmuir.5b01732.

807   [41]   E. Ruiz-Agudo, M. Urosevic, C. V. Putnis, C. Rodríguez-Navarro, C. Cardell, A. Putnis,
808   Ion-specific effects on the kinetics of mineral dissolution, Chem. Geol. 281 (2011) 364–
809   371. https://doi.org/10.1016/j.chemgeo.2011.01.003.

810   [42]   T. Yang, W. Huh, J.Y. Jho, I.W. Kim, Effects of fluoride and polymeric additives on the
811   dissolution of calcite and the subsequent formation of fluorite, Colloids Surfaces A
812   Physicochem. Eng. Asp. 451 (2014) 75–84.

813   https://doi.org/10.1016/j.colsurfa.2014.03.040.

814 [43] S. Elhadj, E.A. Salter, A. Wierzbicki, J.J. De Yoreo, N. Han, P.M. Dove, Peptide controls

815   on calcite mineralization: Polyaspartate chain length affects growth kinetics and acts as a

816   stereochemical switch on morphology, Cryst. Growth Des. 6 (2006) 197–201.

817 [44] S. Elhadj, J.J. De Yoreo, J.R. Hoyer, P.M. Dove, Role of molecular charge and

818   hydrophilicity in regulating the kinetics of crystal growth, Proc. Natl. Acad. Sci. 103

819   (2006) 19237–19242.

820 [45] K.J. Davis, P.M. Dove, J.J. De Yoreo, The role of Mg2+ as an impurity in calcite growth,

821   Science (80-.). 290 (2000) 1134–1137.

822 [46] E. Ruiz-Agudo, M. Kowacz, C. V. Putnis, A. Putnis, The role of background electrolytes

823   on the kinetics and mechanism of calcite dissolution, Geochim. Cosmochim. Acta. 74

824   (2010) 1256–1267. https://doi.org/10.1016/j.gca.2009.11.004.

825 [47] H.H. Teng, P.M. Dove, Surface site-specific interactions of aspartate with calcite during

826   dissolution: Implications for biomineralization, Am. Mineral. 82 (1997) 878–887.

827   https://doi.org/10.2138/am-1997-9-1005.

828 [48] H. Nada, Difference in the conformation and dynamics of aspartic acid on the flat regions,

829   step edges, and kinks of a calcite surface: A molecular dynamics study, J. Phys. Chem. C.

830   118 (2014) 14335–14345. https://doi.org/10.1021/jp502332c.

831 [49] I. Choi, I.W. Kim, Molecular Dynamics Simulation to Understand the Ability of Anionic

832   Polymers to Alter the Morphology of Calcite, (2017).

833   https://doi.org/10.1155/2017/7594950.

834 [50] J.P. Nicot, A. Gherabati, R. Darvari, P. Mickler, Salinity Reversal and Water Freshening

835   in the Eagle Ford Shale, Texas, USA, ACS Earth Sp. Chem. 2 (2018) 1087–1094.

836   https://doi.org/10.1021/acsearthspacechem.8b00095.

837 [51] J.R. Barnes, H. Dirkzwager, J.R. Smit, J.P. Smit, R.C. Navarrete, B.H. Ellison, M.A.

838   Buijse, Application of internal olefin sulfonates and other surfactants to EOR. Part 1:

839   Structure - Performance relationships for selection at different reservoir conditions, in:

840   SPE - DOE Improv. Oil Recover. Symp. Proc., OnePetro, 2010: pp. 663–678.

841   https://doi.org/10.2118/129766-ms.

842 [52] H. Abdulelah, S. Mahmood, S. Al-Hajri, M. Hakimi, E. Padmanabhan, Retention of

843   Hydraulic Fracturing Water in Shale: The Influence of Anionic Surfactant, Energies. 11

844   (2018) 3342. https://doi.org/10.3390/en11123342.

845   [53] H.H. Teng, Controls by saturation state on etch pit formation during calcite dissolution,

846   Geochim. Cosmochim. Acta. 68 (2004) 253–262. https://doi.org/10.1016/S0016-

847   7037(03)00423-X.

848   [54] C. Amrhein, D.L. Suarez, Procedure for determining sodium-calcium selectivity in

849   calcareous and gypsiferous soils, Soil Sci. Soc. Am. J. 54 (1990) 999–1007.

850   https://doi.org/10.2136/sssaj1990.03615995005400040011x.

851   [55] E. Costa, D. Aquilano, Experimental value of the specific surface energy of the cleavage

852   {10.4} calcite rhombohedron in the presence of its saturated aqueous solution, Crystals. 8

853   (2018) 1–8. https://doi.org/10.3390/cryst8060238.

854   [56] X. Hong, M. Newville, T.S. Duffy, Larch: An Analysis Package for XAFS and Related

855   Spectroscopies Related content High-pressure X-ray absorption fine structure in the

856   diamond anvil cell and its applications in geological materials, J. Phys. Conf. Ser. 430

857   (2013) 12007. https://doi.org/10.1088/1742-6596/430/1/012007.

858   [57] A. Manceau, K.L. Nagy, Quantitative analysis of sulfur functional groups in natural

859   organic matter by XANES spectroscopy, Geochim. Cosmochim. Acta. 99 (2012) 206–

860   223. https://doi.org/10.1016/j.gca.2012.09.033.

861   [58] D.L. Parkhurst, C.A.J. Appelo, Description of input and examples for PHREEQC Version

862   3 — A computer program for speciation, batch-reaction, one-dimensional transport, and

863   inverse geochemical calculations, 2013. https://doi.org/10.1016/0029-6554(94)90020-5.

864   [59] T. Zeng, K.T. Kim, C.J. Werth, L.E. Katz, K.K. Mohanty, Surfactant Adsorption on Shale

865   Samples: Experiments and an Additive Model, Energy and Fuels. 34 (2020) 5436–5443.

866   https://doi.org/10.1021/acs.energyfuels.9b04016.

867   [60] A.W. Adamson, A.P. Gast, Physical chemistry of surfaces, 5th ed., interscience, New

868   York, 1990.

869   [61] J. Botto, S.J. Fuchs, B.W. Fouke, A.F. Clarens, J.T. Freiburg, P.M. Berger, C.J. Werth,

870   Effects of Mineral Surface Properties on Supercritical CO2 Wettability in a Siliciclastic

871   Reservoir, Energy and Fuels. 31 (2017) 5275–5285.

872   https://doi.org/10.1021/acs.energyfuels.6b03336.

873   [62] J. Drelich, J.D. Miller, The effect of solid surface heterogeneity and roughness on the

874   contact angle/drop (bubble) size relationship, J. Colloid Interface Sci. 164 (1994) 252–

875   259.

876   [63]   F.M. Fowkes, W.D. Harkins, The state of monolayers adsorbed at the interface solid—
877   aqueous solution, J. Am. Chem. Soc. 62 (1940) 3377–3386.

878   [64]   M.J. Rosen, J.T. Kunjappu, Surfactants and interfacial phenomena, John Wiley & Sons,
879   2012.

880   [65]   W.A. Ducker, E.J. Wanless, Surface-aggregate shape transformation, Langmuir. 12 (1996)
881   5915–5920. https://doi.org/10.1021/la9605448.

882   [66]   E.J. Wanless, T.W. Davey, W.A. Ducker, Surface aggregate phase transition, Langmuir.
883   13 (1997) 4223–4228. https://doi.org/10.1021/la970146k.

884   [67]   R.E. Lamont, W.A. Ducker, Surface-induced transformations for surfactant aggregates, J.
885   Am. Chem. Soc. 120 (1998) 7602–7607. https://doi.org/10.1021/ja9742895.

886   [68]   F. Jiménezjiménez-A´ Ngeles, A. Khoshnood, A. Firoozabadi, Molecular Dynamics
887   Simulation of the Adsorption and Aggregation of Ionic Surfactants at Liquid−Solid
888   Interfaces, (2017). https://doi.org/10.1021/acs.jpcc.7b09466.

889   [69]   A.S. Lea, J.E. Amonette, D.R. Baer, Y. Liang, N.G. Colton, Microscopic effects of
890   carbonate, manganese, and strontium ions on calcite dissolution, Geochim. Cosmochim.
891   Acta. 65 (2001) 369–379.

892   [70]   Z. Chen, Z. Nan, Controlling the polymorph and morphology of CaCO3 crystals using
893   surfactant mixtures, J. Colloid Interface Sci. 358 (2011) 416–422.
894   https://doi.org/10.1016/j.jcis.2011.02.062.

895   [71]   K.K. Sand, C.S. Pedersen, S. Sjöberg, J.W. Nielsen, E. Makovicky, S.L.S. Stipp,
896   Biomineralization: Long-term effectiveness of polysaccharides on the growth and
897   dissolution of calcite, Cryst. Growth Des. 14 (2014) 5486–5494.
898   https://doi.org/10.1021/cg5006743.

899   [72]   K. Miyata, J. Tracey, K. Miyazawa, V. Haapasilta, P. Spijker, Y. Kawagoe, A.S. Foster,
900   K. Tsukamoto, T. Fukuma, Dissolution Processes at Step Edges of Calcite in Water
901   Investigated by High-Speed Frequency Modulation Atomic Force Microscopy and
902   Simulation, Nano Lett. 17 (2017) 4083–4089.
903   https://doi.org/10.1021/acs.nanolett.7b00757.

904   [73]   J.-W. Shen, C. Li, N.F.A. Van Der Vegt, C. Peter, Understanding the Control of
905   Mineralization by Polyelectrolyte Additives: Simulation of Preferential Binding to Calcite

906   Surfaces, (2013). https://doi.org/10.1021/jp402341w.

907   [74]   P. Van Cappellen, L. Charlet, W. Stumm, P. Wersin, A surface complexation model of the

908   carbonate mineral-aqueous solution interface, Geochim. Cosmochim. Acta. 57 (1993)

909   3505–3518. https://doi.org/10.1016/0016-7037(93)90135-J.

910   [75]   J. Song, S. Rezaee, L. Zhang, Z. Zhang, M. Puerto, O.B. Wani, F. Vargas, S. Alhassan,

911   S.L. Biswal, G.J. Hirasaki, Characterizing the Influence of Organic Carboxylic Acids and

912   Inorganic Silica Impurities on the Surface Charge of Natural Carbonates Using an

913   Extended Surface Complexation Model, (2019).

914   https://doi.org/10.1021/acs.energyfuels.8b03896.

915   [76]   M. Tagavifar, S.H. Jang, H. Sharma, D. Wang, L.Y. Chang, K. Mohanty, G.A. Pope,

916   Effect of pH on adsorption of anionic surfactants on limestone: Experimental study and

917   surface complexation modeling, Colloids Surfaces A Physicochem. Eng. Asp. 538 (2018)

918   549–558. https://doi.org/10.1016/j.colsurfa.2017.11.050.

919   [77]   C. Geffroy, A. Foissy, J. Persello, B. Cabane, Surface complexation of calcite by

920   carboxylates in water, J. Colloid Interface Sci. 211 (1999) 45–53.

921   https://doi.org/10.1006/jcis.1998.5966.

922   [78]   O.S. Pokrovsky, J. Schott, Processes at the magnesium-bearing carbonates/solution

923   interface. II. Kinetics and mechanism of magnesite dissolution, Geochim. Cosmochim.

924   Acta. 63 (1999) 881–897. https://doi.org/10.1016/S0016-7037(99)00013-7.

925   [79]   M. Bruno, F.R. Massaro, L. Pastero, E. Costa, M. Rubbo, M. Prencipe, D. Aquilano, New

926   estimates of the free energy of calcite/water interfaces for evaluating the equilibrium

927   shape and nucleation mechanisms, Cryst. Growth Des. 13 (2013) 1170–1179.

928   https://doi.org/10.1021/cg3015817.

929

930 **Table 1. Mineralogy and total organic matter content of Eagle Ford shale sample.**

Mineral	Chemical Formula	Eagle Ford Shale
Calcite	$CaCO_3$	67.5%
Dolomite	$CaMg(CO_3)_2$	0%
Siderite	FeCO3	0.2%
Apatite	$Ca5(PO_4)_3OH$	0.7%
Pyrite	FeS_2	1.3%
Quartz	SiO_2	8.7%
K-Feldspar	$KAlSi_3O_8$	5.0%
Plagioclase	$NaAlSi_3O_8$-$CaAl_2Si_2O_8$	4.1%
Total Clays	Clay constituents below	11.6%
Chlorite		0.5%
Kaolinite		0.7%
Illte/Mica		6.2%
Mixed Illite/Smectite		4.2%
Total Organic Carbon		3.7 mg/g

931

Table 2. Contact angles, interfacial tensions, and adsorbed IOS

Parameter	Brine		IOS 500		IOS 3000	
	Fresh	Aged	Fresh	Aged	Fresh	Aged
Brine-Calcite Contact Angle*	72.9 ±5.4°	42.5 ±10.5	38.8 ±4.0°	22.5 ±3.8	20.5 ±1.9°	10.7 ±2.2
Brine-Air Surface Tension [mJ/m²]**	71.9±0.4		28.1±0.9		26.6±0.01	
Brine-Calcite Interfacial Tension [mJ/m²]#	443	411	442	438	439	438
Surface Pressure [mJ/m²]##	NA	NA	-0.9‡	27	-0.2‡	27

*The left and right sides of five drops on calcite were evaluated for each measurements. **Pendant drop method. #Based on Young's relation ($\gamma_{LV}\cos\theta = \gamma_{SV} - \gamma_{SL}$). The surface tension of calcite with air is 464 mJ/m² from Bruno et al. [79]. ##From Fowkes and Harkins [63] ($F = \gamma_{LV,IOSBrine}\cos\theta_{IOSBrine} - \gamma_{LV,Brine}\cos\theta_{Brine}$). ‡These values result from subtracting one large number from another, and are not significantly different from zero. Therefore, these two surface pressures are too small for accurate quantification.

Table 3. Calcite pit angles.

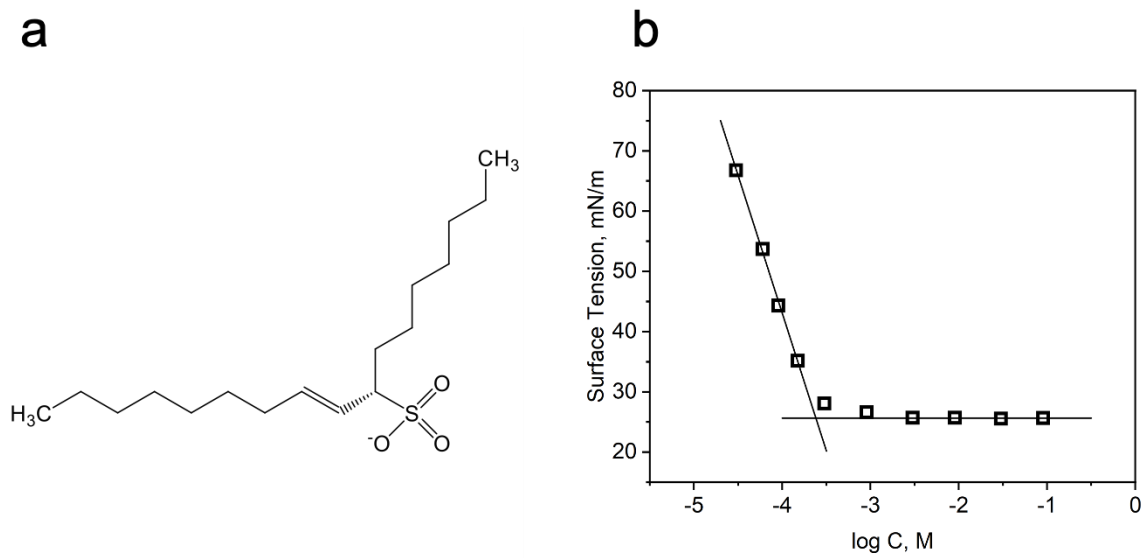| Angle	Brine		IOS 500		IOS 3000	
	i	ii	iii	iv	v	vi
Pit Angle from Adjacent Horizontal at Acute Edge	6.2°	6.2°	0.5°	0.6°	0.6°	0.7°
Pit Angle from Adjacent Horizontal at Obtuse Edge	53.4°	55.6°	0.8°	0.9°	1.0°	1.9°

Table 4. Binding energies of the IOS molecule at different Calcite sites.

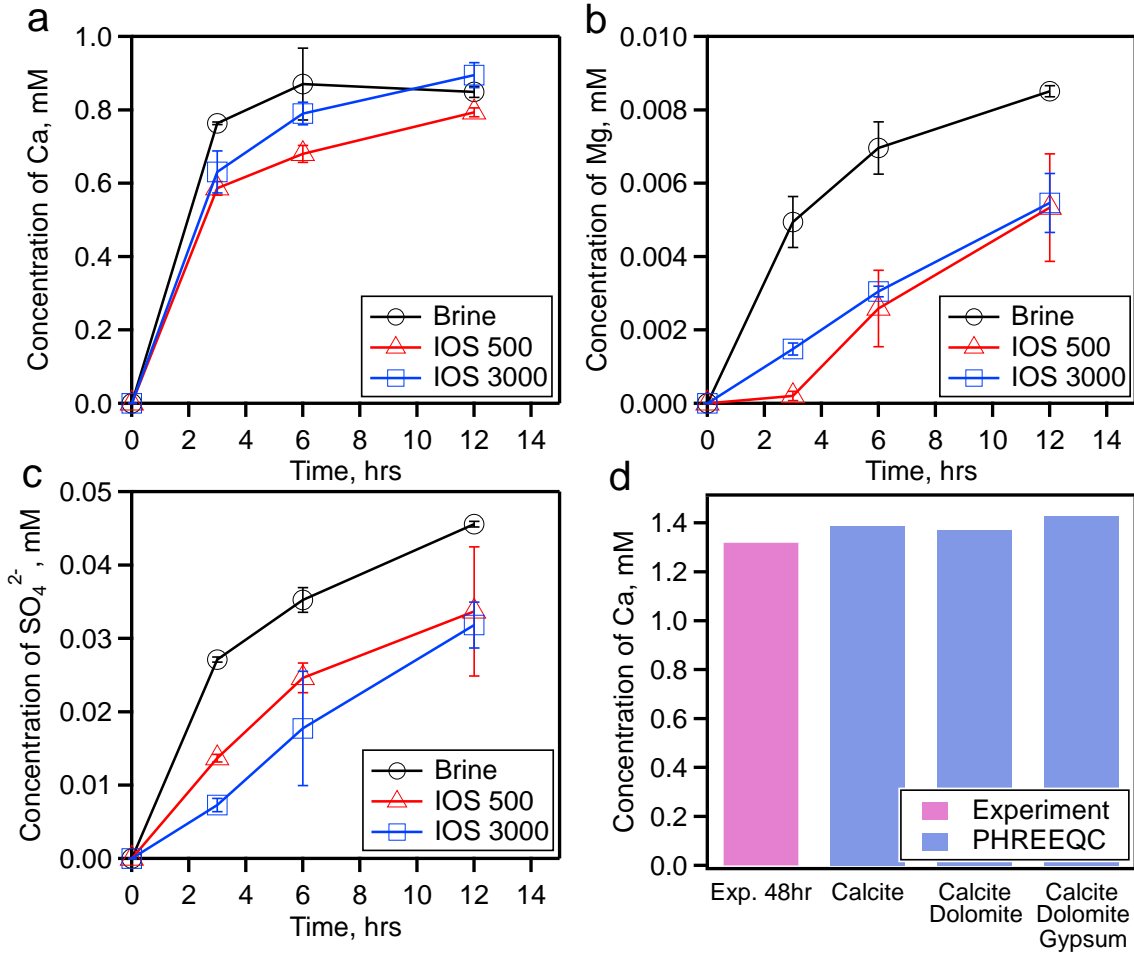| Binding energies (eV)	Terrace site	Obtuse step	Acute step
Vacuum	-0.78	-2.38	-3.51
Solvent	-0.28	-0.94	-1.02

948

Figure 1. a) Representative structure of IOS (n=17), b) surface tension as a function of log molar

concentration of IOS in brine (0.4 M KCl) at room temperature.

951

34

952

953

Figure 2. a) Ca, b) Mg, and c) SO_4^{2-} release into solution from Eagle Ford Shale after aging in brine or IOS brine for 12 hours. Initial pH of the solution is 6.3, and ionic strength of brine is 0.4 M. All experiments were run in triplicate, and error bar represents standard deviation. d) PHREEQC modeling results showing potential mineral contributions to Ca concentrations. IOS 500 and IOS 3000 refer to brine with either 500 or 3000 mg/L of IOS added.

959
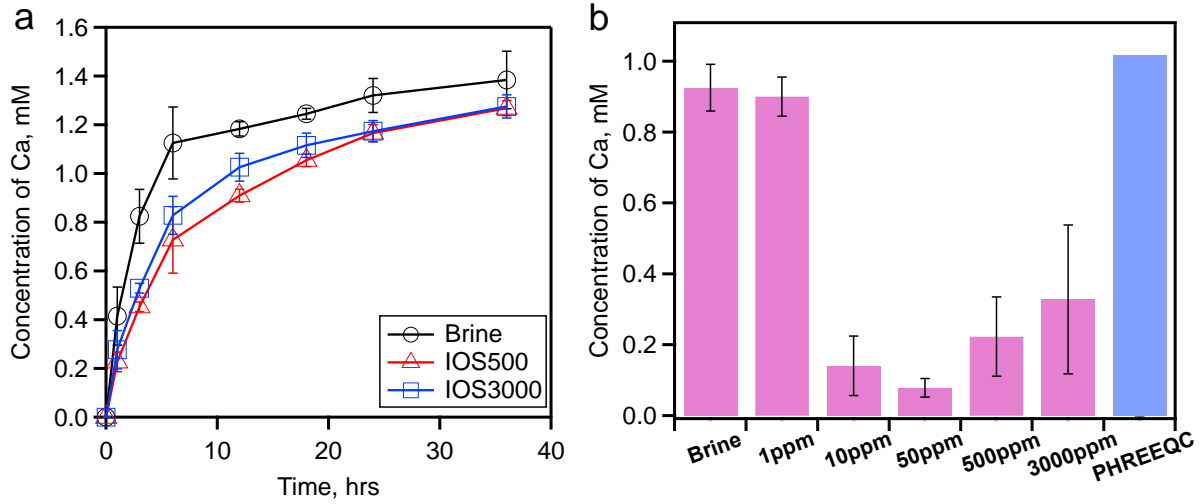
Figure 3. a) Transient Ca release into solution from calcite particles (150-850 μm) after aging in brine or IOS brine for 36 hours. b) Ca release into solution for cleaved calcite piece after aging in brine or IOS brine for 12 hours, along with PHREEQC model results showing simulated equilibrium Ca concentration. IOS 500 and IOS 3000 refer to brine with either 500 or 3000 mg/L of IOS added. Initial pH of the solution is 6.3, and ionic strength of brine is 0.4 M. All experiments were run in triplicate, and error bar represents standard deviation.
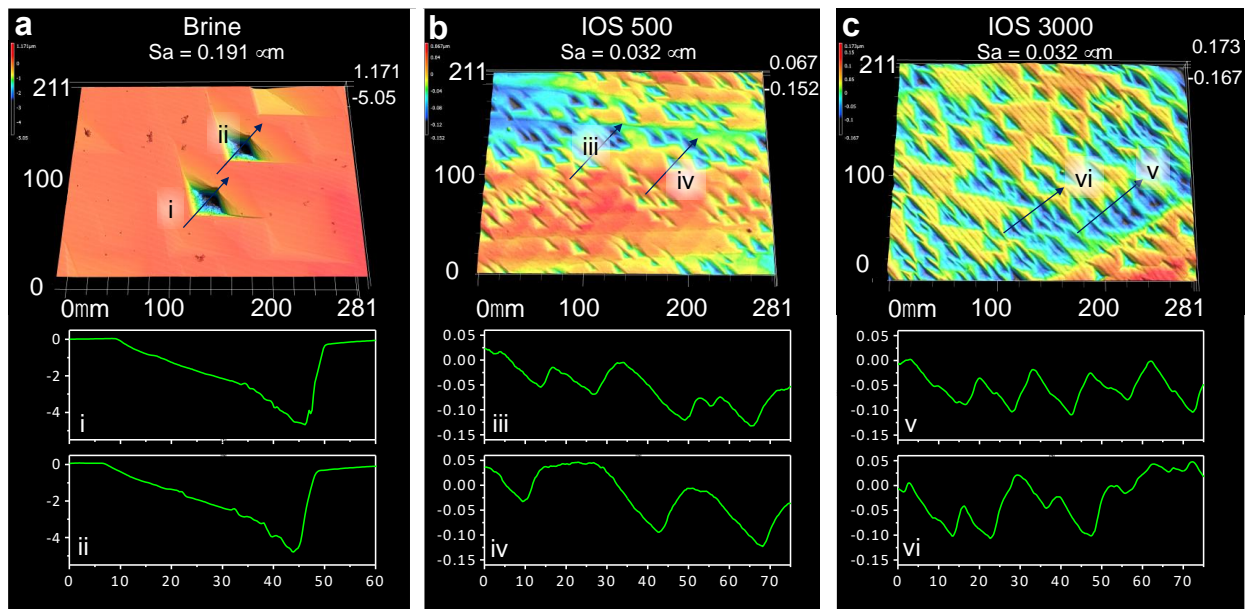
Figure 4. Laser profilometry results showing etch pits on freshly cleaved calcite surfaces aged in a) brine or b) IOS brine for 12 hours. IOS 500 and IOS 3000 refer to brine with either 500 or 3000 mg/L of IOS added. Arithmetic average areal surface roughness (S_a) is provided on top of each surface profile. All the numbers in this figure are in μm.

37

974
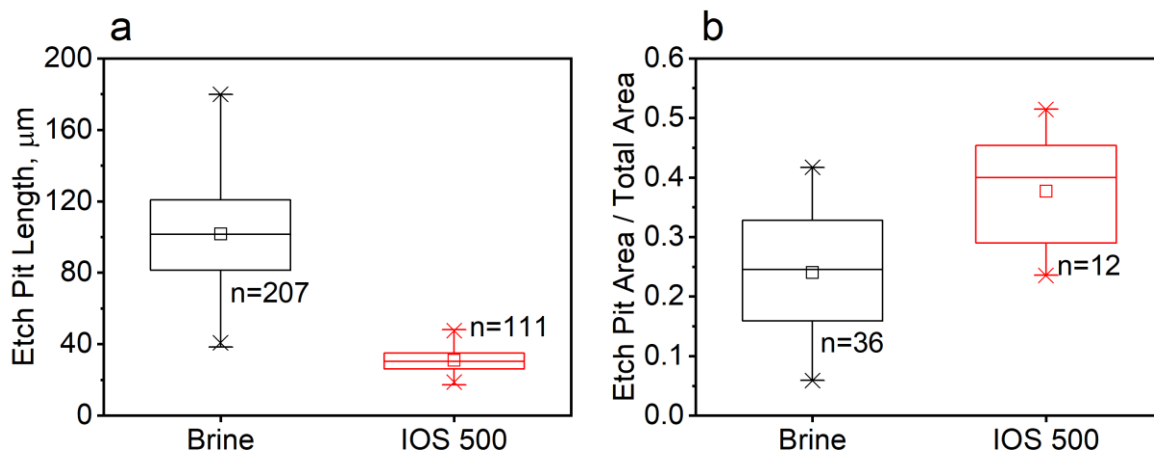
Figure 5. Box plots showing a) etch pit lengths and b) fraction of calcite surface area occupied by
etch pits, both after 12 hours of aging in brine without (Brine) or with (IOS 500) IOS surfactant at
500 mg/L. Box plot lines represent median, 25th, and 75th percentile values plus outliers, with mean
values shown by a square symbol.

979

980

Figure 6. Laser profilometry results showing etch pits on freshly cleaved calcite surfaces a) aged for two sequential 12 hour periods in brine only, and b) aged for two sequential 12 hour periods with brine first, and then in IOS brine. IOS 500 refer to brine with 500 mg/L of IOS added. Arithmetic average areal surface roughness (S_a) is provided on top of each surface profile. All the numbers shown in this figure are in μm.
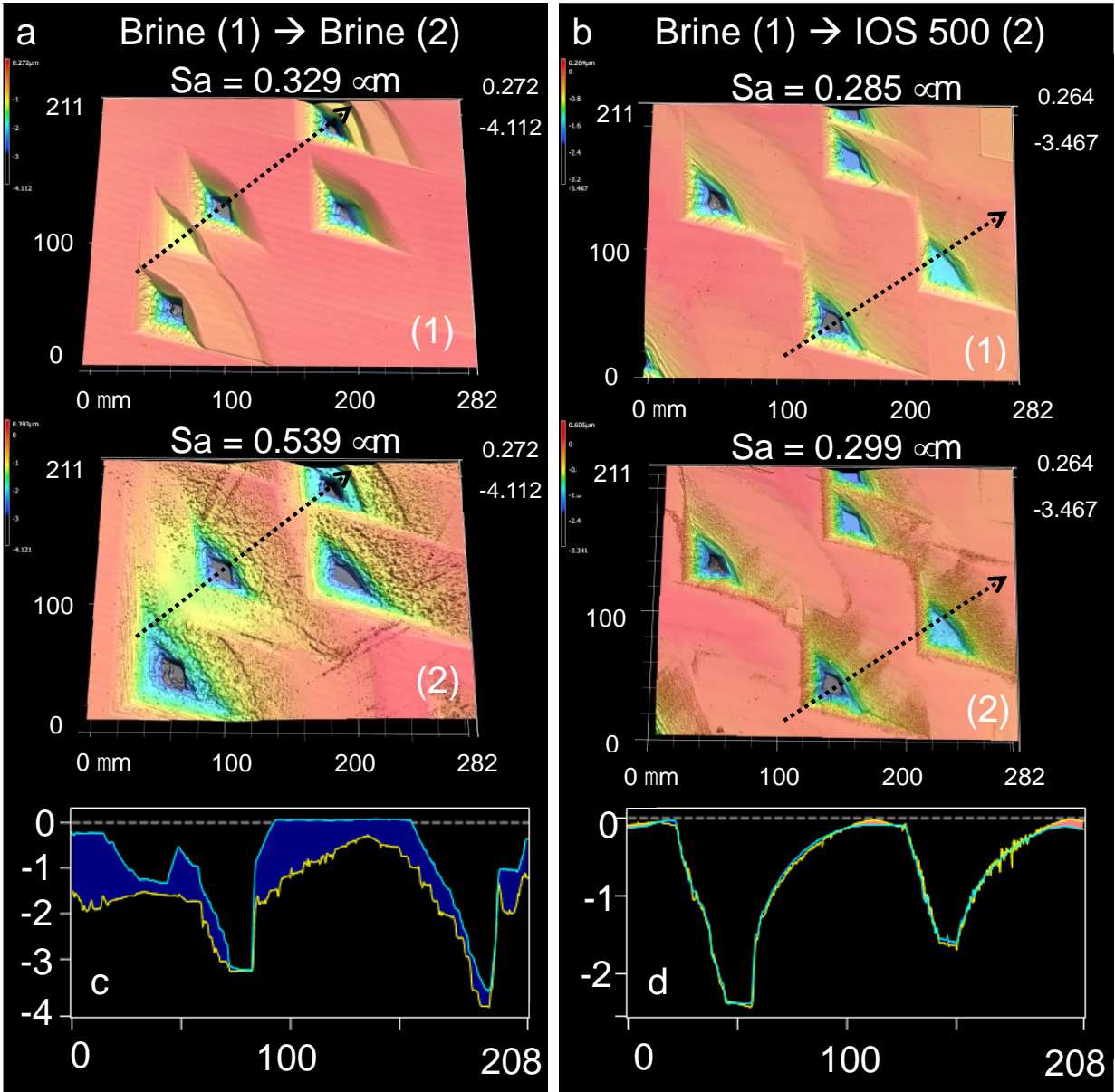
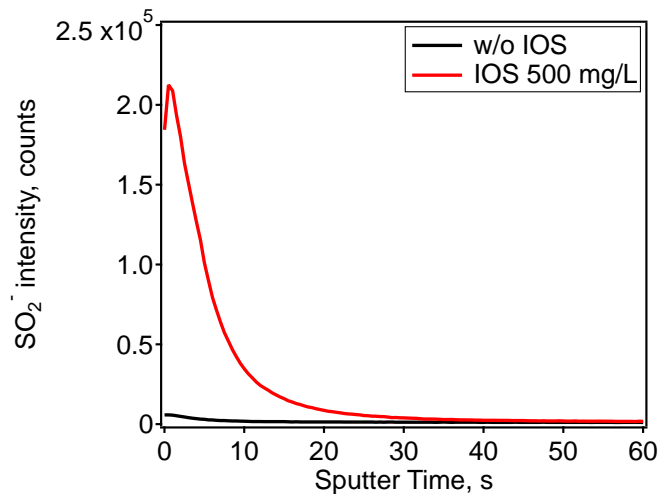**Figure 7**. Background CO_3^- normalized SO_2^- ToF-SIMS profiles of calcite under two different conditions. Solid black line is a sample without IOS, whereas red line is a sample dried after exposure to IOS 500 for 1hr.
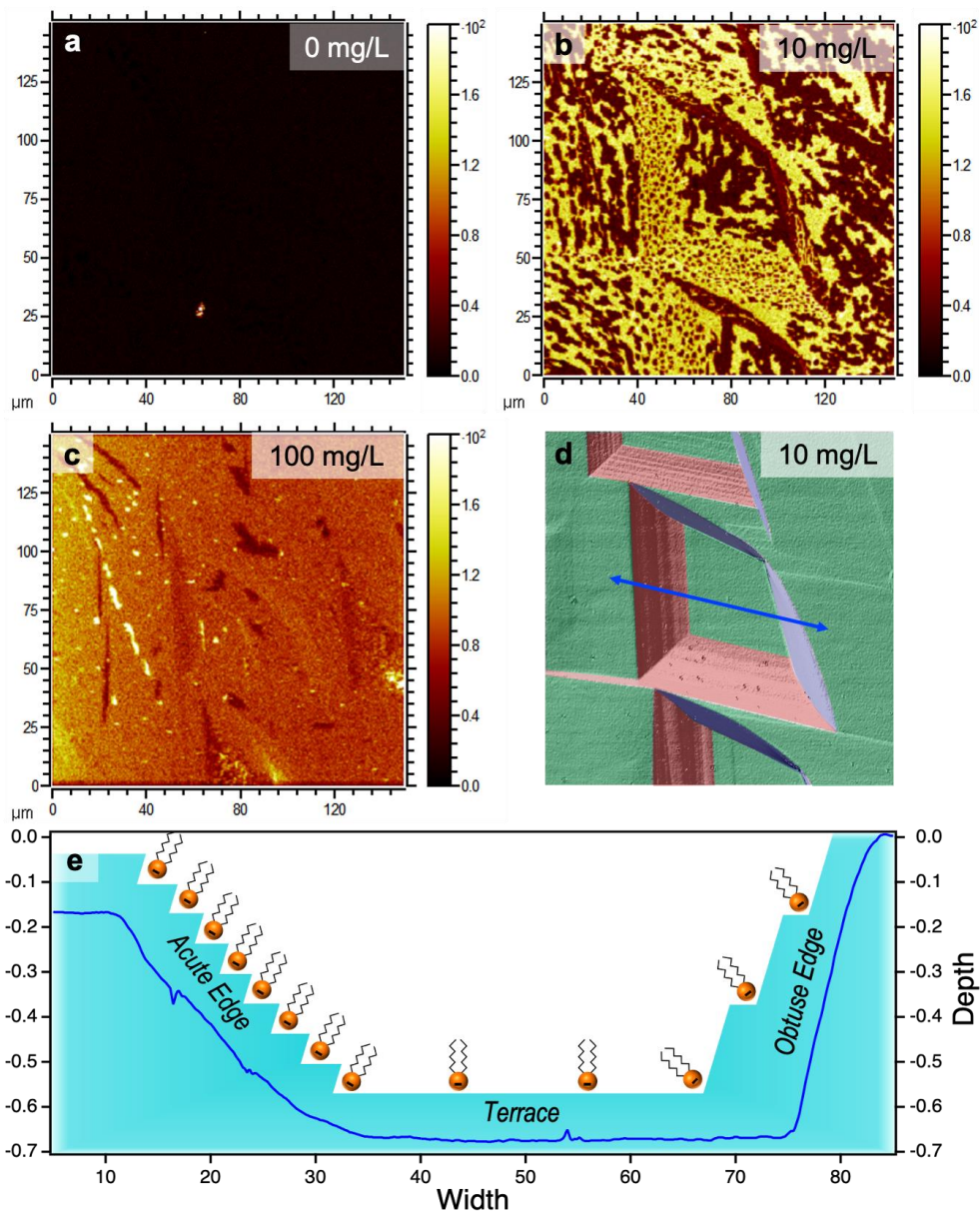
Figure 8. ToF-SIMS 2D(XY) images of SO_2^- distribution on calcite surfaces after a) aging in only brine for 12 hours and then drying, b-c) aging in only brine for 12 hours, followed by 10 and 100 mg/L IOS addition, respectively for an additional 1 hour, and then drying, d) comparison of laser profilometer result and corresponding b) ToF-SIMS 2D(XY) image of SO_2^-; green, red, and blue shades correspond to terrace, acute edges, and obtuse edges, respectively, e) schematic representation of IOS adsorbed on the calcite surface; surface profile (blue line) shown in e) corresponds to the blue line in d).
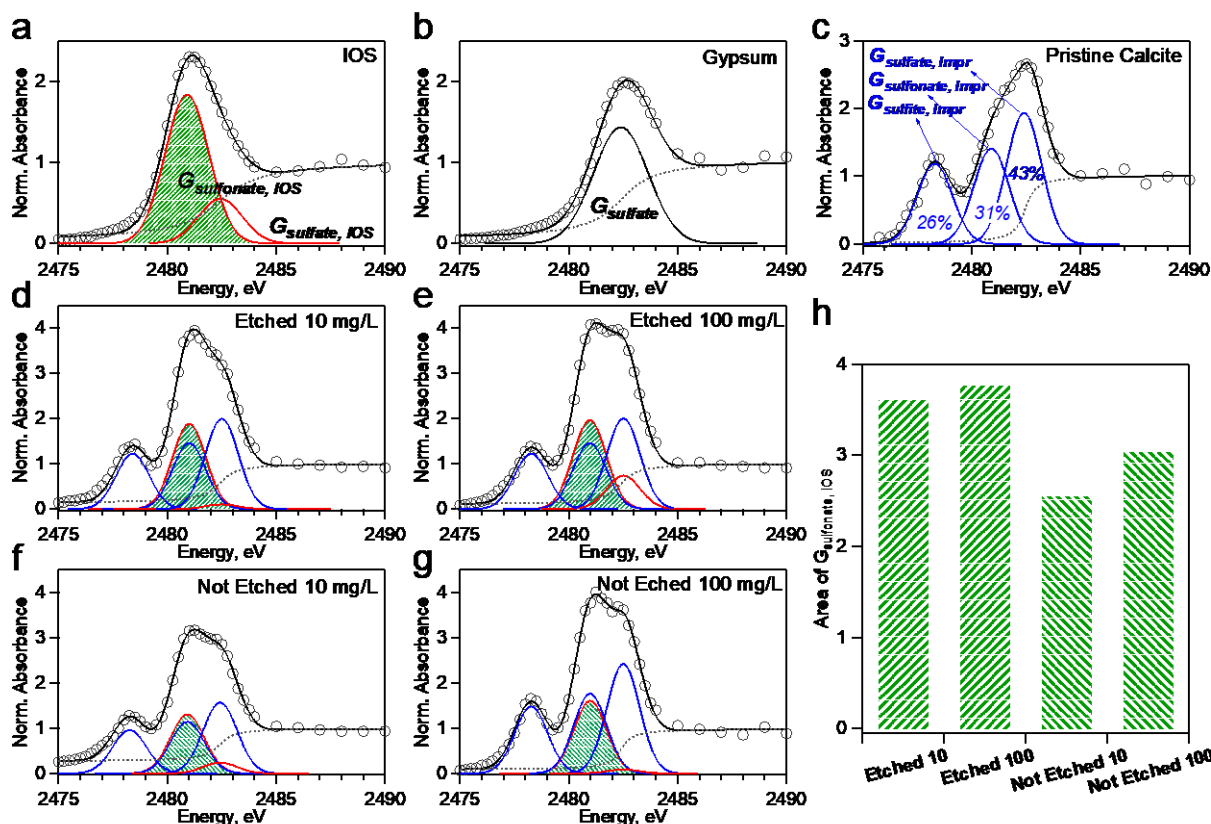
1001

Figure 9. Sulfur K-edge NEXAFS spectra of: a) A drop of concentrated IOS solution (30.1 %) on a silicon wafer. b) Freshly cleaved gypsum without further treatment. c) Freshly cleaved calcite without further treatment. d-e) Freshly cleaved calcite aged in only brine for 12 hours, followed by aging for 1 more hour in brine mixed with either 10 and 100 mg/L IOS, and then dried. f-g) Freshly cleaved calcite aged in calcite-saturated brine for 12 hours to prevent pit formation, followed by aging for 1 more hour in brine mixed with either 10 and 100 mg/L IOS, and then dried. h) Decomposed peak areas of $G_{sulfonate, IOS}$ (green shaded area of d-g) showing relative amounts of IOS adsorbed to the calcite. Gaussian-Arctan fitting parameters are summarized in Table S5 (Supporting Information).
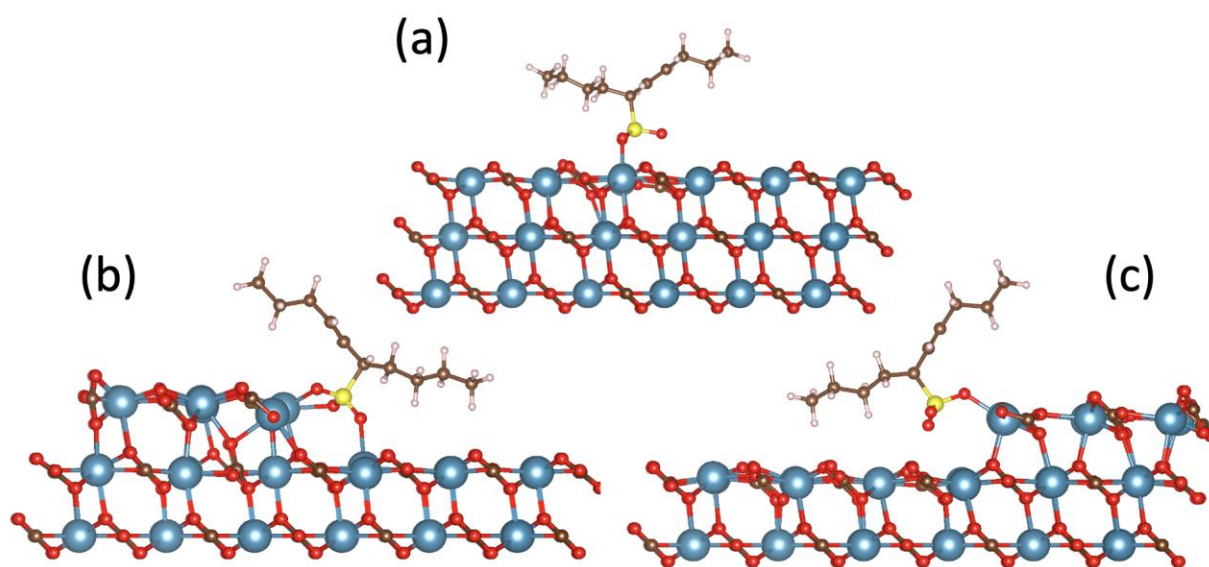
Figure 10. Side view of IOS adsorption at (a) terrace, (b) acute step and (c) obtuse step sites on the calcite $\{10\bar{1}4\}$ surface.

1015 **Graphical Abstract**
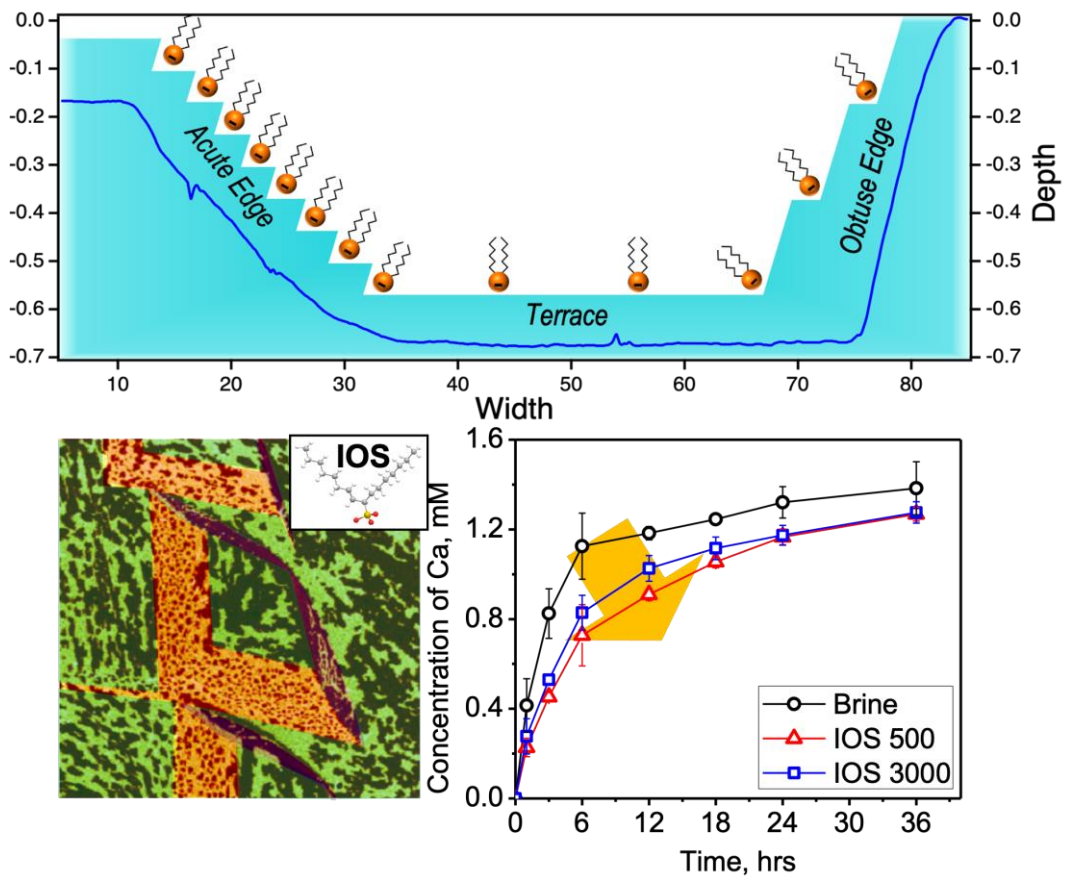
1016
1017

Surfactant Inhibition Mechanisms of Carbonate Mineral Dissolution in Shale

Kyung Tae Kim[1], Mantha Sai Pavan Jagannath[3], Gregory M. Su[4], Guillaume Freychet[5], Tongzhou Zeng[2], Kishore K. Mohanty[2], Graeme Henkelman[3], Lynn E. Katz[1], Charles J. Werth[1,*]

[1] 301 East Dean Keeton St., Department of Civil, Architecture & Environmental Engineering, University of Texas at Austin, Austin, TX, 78721, USA

[2] 200 East Dean Keeton St., Hildebrand Department of Petroleum & Geosystems Engineering, University of Texas at Austin, Austin, TX, 78721, USA

[3] 2506 Speedway Dr., Department of Chemistry, University of Texas at Austin, Austin, TX, 78721, USA

[4] Advanced Light Sources, Lawrence Berkeley National Laboratory, Berkeley, CA 94720, USA

[5] National Synchrotron Light Source II, Brookhaven National Laboratory, Upton, NY, 11973, USA

*corresponding author: werth@utexas.edu

1. ToF-SIMS Analyses.

The Bi_3^+ was chosen to reduce the mixing induced by sputtering of Cs^+ and to enhance the yield of organic secondary ions. For depth profiling, a 300×300 μm^2 area was raster scanned with the sputtering beam while a 100×100 μm^2 area was raster scanned with the analysis beam within the regressing sputtered area. For higher-resolution imaging, a 500×500 μm^2 area was raster scanned with the sputtering beam while a 150×150 μm^2 area was raster scanned with burst-alignment mode. The high-resolution 2D (XY) images were obtained by overlapping 700 layers of scanning results (i.e., SO_2^-). All samples were degassed overnight under vacuum pressure of $<10^{-8}$ torr before analysis, and approximately 2×10^{-6} torr of Ar was used as a discharge medium during the ToF-SIMS analysis/sputtering process. All secondary ions had negative polarity.

2. Surface excess concentration and minimum area per molecule

Surface excess concentration of IOS (Γ) in mole/cm^2 at the interface of water and air was first calculated from following Equation S1. Surface excess concentration of IOS was calculated based on the surface tension measurement as a function of surfactant concentration in Figure S1b.

$$\Gamma = -\frac{1}{2.303yRT}\left(\frac{\partial\gamma}{\partial logC}\right)_T \tag{S1}$$

Where $[\partial\gamma/(\partial \log C)]_T$ is the slope (Figure S1b), T is absolute temperature, R = 8.31 J·mol^{-1}·K^{-1} and $y = 1 + C_{IOS}/(C_{IOS} + C_{KCl})$. To compensate for ionic strength of the brine (0.4 M KCl), $\partial logC$ was replaced by $\partial(logC + logf_{IOS})$, and f_{IOS} was calculated by using Debye-Hückel equation (Equation S2),

$$logf_{IOS} = -\frac{0.509Z_{IOS}^2\sqrt{I}}{1 + 0.33\alpha\sqrt{I}} \tag{S2}$$

Where I is ionic strength of the solution, α is taken as 0.6 for IOS. Ionic strength of brine was calculated by PHREEQC. Concentration of IOS was not considered in ionic strength calculation because the maximum concentration of IOS used to calculate $[\partial\gamma/(\partial \log C)]_T$ was less than 10^{-3}

M. Surface excess concentration was then converted to minimum area per molecule A_{min} in Å^2 by Equation S3.

$$A_{min} = \frac{10^{16}}{N\Gamma} \tag{S3}$$

Calculated excess surface concentration Γ and minimum area per molecule A_{min} are 8.01 mole/cm^2 and 20.7 Å^2, respectively.
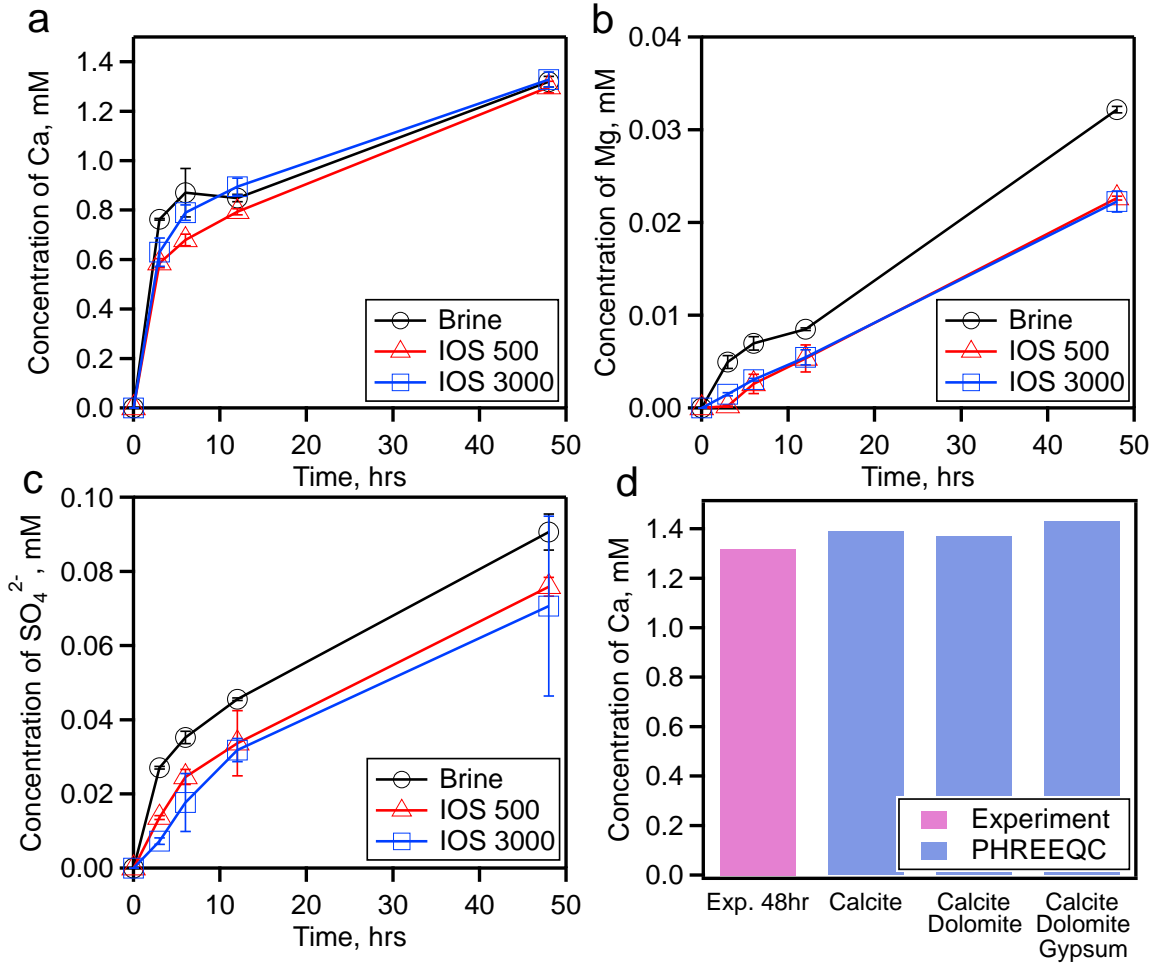
Figure S1. a) Ca, b) Mg, and c) SO$_4^{2-}$ release into solution from Eagle Ford Shale after aging in brine or IOS brine for 48 hours. Initial pH of the solution is 6.3, and ionic strength of brine is 0.4 M. All experiments were run in triplicate, and error bar represents standard deviation. d) PHREEQC modeling results showing potential mineral contributions to Ca^{2+} concentrations. IOS 500 and IOS 3000 refer to brine with either 500 or 3000 mg/L of IOS added.
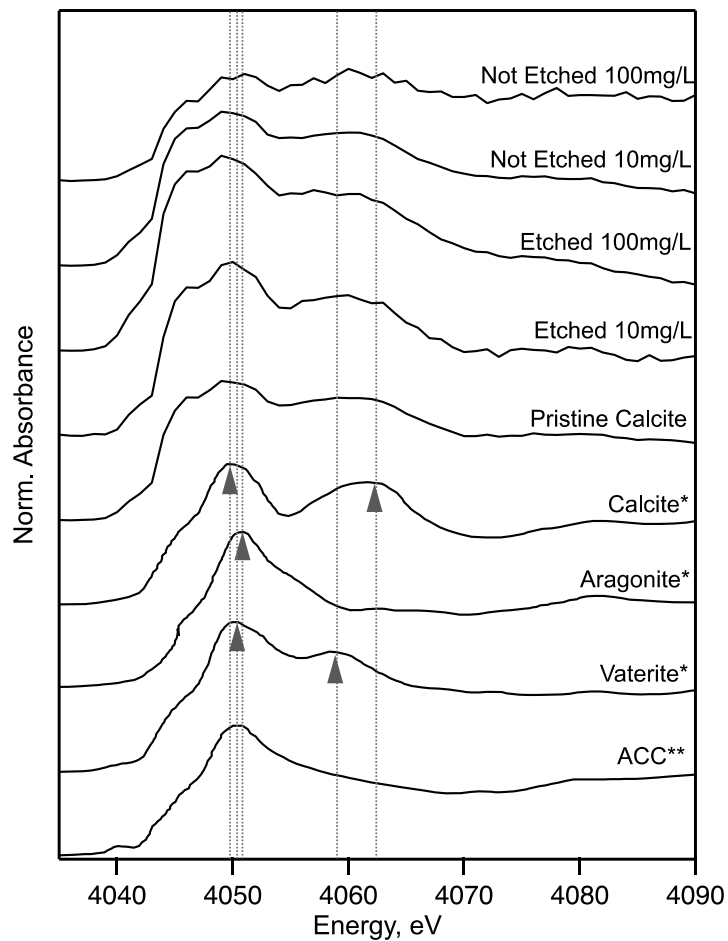
Figure S2. Calcium K-edge NEXAFS spectra of 5 samples in Figure 8 and reference spectra of calcite polymorphs. Reference spectra annotated with * and ** were reproduced from Hayakawa et al. and Politi et al., respectively [1,2].

Table S1. List of dissolution/precipitation and complexation reactions used in the PHREEQC.

Reaction (phreeqc.dat)			Log K
$CaCO_3(S)$	$\Leftrightarrow$	$Ca^{2+} + CO_3^{2-}$	-8.48
$CaMg(CO_3)_2(S)$	$\Leftrightarrow$	$Ca^{2+} + Mg^{2+} + 2CO_3^{2-}$	-17.09
$CaSO_4 \cdot 2H_2O(S)$	$\Leftrightarrow$	$Ca^{2+} + SO_4^{2-} + 2H_2O$	-4.58
$CO_2(g)$	$\Leftrightarrow$	$CO_2(aq)$	-1.468
$CO_3^{2-} + H^+$	$\Leftrightarrow$	HCO_3^-	10.329
$CO_3^{2-} + 2H^+$	$\Leftrightarrow$	$CO_2 + H_2O$	16.681
$Ca^{2+} + CO_3^{2-}$	$\Leftrightarrow$	$CaCO_3$	3.224
$Ca^{2+} + CO_3^{2-} + H^+$	$\Leftrightarrow$	$CaHCO_3^+$	11.435
$Ca^{2+} + SO_4^{2-}$	$\Leftrightarrow$	$CaSO_4$	2.25
$Ca^{2+} + HSO_4^-$	$\Leftrightarrow$	$CaHSO_4^+$	1.08
$Ca^{2+} + H_2O$	$\Leftrightarrow$	$CaOH^+ + H^+$	-12.78

Table S2. Ca speciation for Eagle Ford shale at 48 hours for three different modeling cases.

Calcite						
	Molality	Activity	Log Molality	Log Activity	Log γ	Fraction (%)
ToTCa	1.39×10^{-3}					
Ca^{2+}	1.37×10^{-3}	3.73×10^{-4}	-2.86	-3.43	-0.57	98.775
$CaHCO_3^+$	1.24×10^{-5}	8.88×10^{-6}	-4.91	-5.05	-0.14	0.890
$CaCO_3$	4.97×10^{-6}	5.46×10^{-6}	-5.30	-5.26	0.04	0.358
$CaOH^+$	8.92×10^{-9}	6.53×10^{-9}	-8.05	-8.19	-0.14	0.001
Calcite + Dolomite						
	Molality	Activity	Log Molality	Log Activity	Log g	Fraction (%)
ToTCa	1.37×10^{-3}					
Ca^{2+}	1.35×10^{-3}	3.68×10^{-4}	-2.87	-3.44	-0.57	98.757
$CaHCO_3^+$	1.23×10^{-5}	8.81×10^{-6}	-4.91	-5.06	-0.14	0.896
$CaCO_3$	4.97×10^{-6}	5.46×10^{-6}	-5.30	-5.26	0.04	0.363
$CaOH^+$	8.86×10^{-9}	6.48×10^{-9}	-8.05	-8.19	-0.14	0.001
Calcite + Dolomite + Gypsum						
	Molality	Activity	Log Molality	Log Activity	Log g	Fraction (%)
ToTCa	1.43×10^{-3}					
Ca^{2+}	1.41×10^{-3}	3.83×10^{-4}	-2.85	-3.42	-0.57	98.738
$CaHCO_3^+$	1.25×10^{-5}	8.99×10^{-6}	-4.90	-5.05	-0.14	0.877
$CaCO_3$	4.97×10^{-6}	5.46×10^{-6}	-5.30	-5.26	0.04	0.349
$CaSO_4$	7.61×10^{-7}	8.35×10^{-7}	-6.12	-6.08	0.04	0.053
$CaOH^+$	9.04×10^{-9}	6.62×10^{-9}	-8.04	-8.18	-0.14	0.001
$CaHSO_4^+$	6.82×10^{-14}	4.99×10^{-14}	-13.17	-13.30	-0.14	0.000

Table S3. Dissolution terms for Eagle Ford shale at various time points.

Parameter time=	0 hrs	3 hrs	6 hrs	12 hrs	48 hrs
pH	6.30	7.95	7.98	7.95	8.03
Alk [mequiv./kg]	0.10	2.63	2.73	2.71	2.88
a_{H^+} [M]	5.01×10^{-7}	1.69×10^{-8}	1.56×10^{-8}	1.71×10^{-8}	9.65×10^{-9}
$a_{Ca^{2+}}$ [M]		2.09×10^{-4}	2.40×10^{-4}	2.37×10^{-4}	3.76×10^{-4}
$a_{CO_3^{2-}}$ [M]	6.24×10^{-9}	2.89×10^{-6}	3.54×10^{-6}	3.18×10^{-6}	8.67×10^{-6}
$a_{HCO_3^-}$ [M]	7.10×10^{-5}	1.11×10^{-3}	1.26×10^{-3}	1.23×10^{-3}	1.90×10^{-3}
$a_{H_2CO_3^*}$ [M]	8.44×10^{-5}	4.45×10^{-5}	4.66×10^{-5}	4.99×10^{-5}	4.34×10^{-5}
SI (Log(Q/K$_{SP}$))		-0.76	-0.61	-0.66	-0.02
k_1 [cm/s]	4.93×10^{-2}	-	-	-	-
k_2 [cm/s]	2.89×10^{-5}	-	-	-	-
k_3 [cm/s]	1.16×10^{-7}	-	-	-	-
k_4 [cm^4/mmol·s]	3.05×10^{-1}	3.02×10^{-1}	3.02×10^{-1}	3.02×10^{-1}	3.02×10^{-1}
$k_1 a_{H^+}$ [mmol/cm^2·s]	2.47×10^{-8}	8.34×10^{-10}	7.71×10^{-10}	8.41×10^{-10}	4.76×10^{-10}
$k_2 a_{H_2CO_3^*}$ [mmol/cm^2·s]	2.43×10^{-9}	1.28×10^{-9}	1.34×10^{-9}	1.44×10^{-9}	1.25×10^{-9}
$k_3 a_{H_2O}$ [mmol/cm^2·s]	1.15×10^{-7}	1.15×10^{-7}	1.15×10^{-7}	1.15×10^{-7}	1.15×10^{-7}
$k_4 a_{Ca^{2+}} a_{HCO_3^{2-}}$ [mmol/cm^2·s]	0	6.99×10^{-8}	9.08×10^{-8}	8.83×10^{-8}	2.16×10^{-7}

Table S4. Dissolution terms for calcite at various time points.

Parameter time=	0 hrs	3 hrs	6 hrs	12 hrs	36 hrs
pH	6.3	8	8.02	8.18	8.24
Alk [mequiv./kg]	0.10	1.71	2.43	2.74	2.89
a_{H^+} [M]	5.01×10^{-7}	1.02×10^{-8}	1.02×10^{-8}	7.46×10^{-9}	6.68×10^{-9}
$a_{Ca^{2+}}$ [M]	0	2.17×10^{-4}	2.95×10^{-4}	3.09×10^{-4}	3.16×10^{-4}
$a_{CO_3^{2-}}$ [M]	6.24×10^{-9}	5.05×10^{-6}	6.74×10^{-6}	9.58×10^{-6}	1.09×10^{-5}
$a_{HCO_3^-}$ [M]	7.10×10^{-5}	1.17×10^{-3}	1.56×10^{-3}	1.62×10^{-3}	1.65×10^{-3}
$a_{H_2CO_3^*}$ [M]	8.44×10^{-5}	2.81×10^{-5}	3.78×10^{-5}	2.87×10^{-5}	2.62×10^{-5}
SI (Log(Q/K$_{SP}$))		-0.5	-0.24	-0.06	0
k_1 [cm/s]	4.93×10^{-2}	-	-	-	-
k_2 [cm/s]	2.89×10^{-5}	-	-	-	-
k_3 [cm/s]	1.16×10^{-7}	-	-	-	-
k_4 [cm^4/mmol·s]	3.05×10^{-1}	3.01×10^{-1}	3.01×10^{-1}	3.01×10^{-1}	3.00×10^{-1}
$k_1 a_{H^+}$ [mmol/cm^2·s]	2.47×10^{-8}	5.00×10^{-10}	5.03×10^{-10}	3.68×10^{-10}	3.3×10^{-10}
$k_2 a a_{H_2CO_3^*}$ [mmol/cm^2·s]	2.43×10^{-9}	8.10×10^{-10}	1.09×10^{-9}	8.28×10^{-10}	7.56×10^{-10}
$k_3 a_{H_2O}$ [mmol/cm^2·s]	1.15×10^{-7}	1.15×10^{-7}	1.15×10^{-7}	1.15×10^{-7}	1.15×10^{-7}
$k_4 a_{Ca^{2+}} a_{HCO_3^{2-}}$ [mmol/cm^2·s]	0	7.58×10^{-8}	1.39×10^{-7}	1.51×10^{-7}	1.57×10^{-7}

Table S5. Summary of Gaussian-Arctan fitting parameters and atomic fraction (%) shown in Figure 9.

		IOS					Gypsum					Pristine Calcite				
		Energy	Width	Amp	Area	%	Energy	Width	Amp	Area	%	Energy	Width	Amp	Area	%
Arctan		2482.4	1.46	1			2482.4	1.17	1			2482.4	0.36	1.02		
Sulfite	$G_{sulfite, Impr}$											2478.3	**1.14**	1.18	2.40	26.1
Sulfonate	$G_{sulfonate, Impr}$											2480.9	**1.14**	1.41	2.86	31.1
	$G_{Sulfonate, IOS}$	2480.9	**1.42**	1.84	4.64	76.9										
Sulfate	$G_{sulfate, Impr}$						2482.4	1.78	1.44	4.53	100	2482.4	**1.14**	1.94	3.92	42.7
	$G_{Sulfate, IOS}$	2482.4	**1.42**	0.55	1.40	23.1										

		Etched 10 mg/L					Etched 100 mg/L				
		Energy	Width	Amp	Area	%	Energy	Width	Amp	Area	%
Arctan		2482.4	0.58	0.89			2482.4	0.57	0.92		
Sulfite	$G_{sulfite, Impr}$	2478.3	**1.08**	1.22	2.34	18.3	2478.3	**1.08**	1.22	2.35	16.6
Sulfonate	$G_{sulfonate, Impr}$	2481.0	**1.08**	1.45	2.78	21.8	2481.0	**1.08**	1.46	2.80	19.7
	$G_{Sulfonate, IOS}$	2481.0	**1.08**	1.89	3.61	28.3	2481.0	**1.08**	1.96	3.77	26.6
Sulfate	$G_{sulfate, Impr}$	2482.5	**1.08**	2.00	3.82	30.0	2482.5	**1.08**	2.00	3.84	27.1
	$G_{Sulfate, IOS}$	2482.5	**1.08**	0.10	0.19	1.5	2482.5	**1.08**	0.74	1.42	10.0

		Not Etched 10 mg/L					Not Etched 100 mg/L				
		Energy	Width	Amp	Area	%	Energy	Width	Amp	Area	%
Arctan		2482.4	0.50	0.74			2482.4	0.38	0.91		
Sulfite	$G_{sulfite, Impr}$	2478.3	**1.11**	0.96	1.88	18.4	2478.3	**1.07**	1.48	2.80	20.1
Sulfonate	$G_{sulfonate, Impr}$	2480.9	**1.11**	1.14	2.24	21.9	2481.0	**1.07**	1.76	3.33	24.0
	$G_{Sulfonate, IOS}$	2480.9	**1.11**	1.30	2.56	25.0	2481.0	**1.07**	1.61	3.04	21.8
Sulfate	$G_{sulfate, Impr}$	2482.4	**1.11**	1.57	3.08	30.1	2482.5	**1.07**	2.42	4.57	32.9
	$G_{Sulfate, IOS}$	2482.4	**1.11**	0.24	0.47	4.6	2482.5	**1.07**	0.09	0.16	1.2

References

[1]   S. Hayakawa, Y. Hajima, S. Qiao, H. Namatame, T. Hirokawa, Characterization of calcium carbonate polymorphs with Ca K edge X-ray absorption fine structure spectroscopy, Anal. Sci. 24 (2008) 835-837.

[2]   Y. Politi, Y. Levi-Kalisman, S. Raz, F. Wilt, L. Addadi, S. Weiner, I. Sagi, Structural characterization of the transient amorphous calcium carbonate precursor phase in sea urchin embryos, Adv. Funct. Mater. 16(2006) 1289-1298.